



저작자표시-동일조건변경허락 2.0 대한민국

이용자는 아래의 조건을 따르는 경우에 한하여 자유롭게

- 이 저작물을 복제, 배포, 전송, 전시, 공연 및 방송할 수 있습니다.
- 이차적 저작물을 작성할 수 있습니다.
- 이 저작물을 영리 목적으로 이용할 수 있습니다.

다음과 같은 조건을 따라야 합니다:



저작자표시. 귀하는 원저작자를 표시하여야 합니다.



동일조건변경허락. 귀하가 이 저작물을 개작, 변형 또는 가공했을 경우에는, 이 저작물과 동일한 이용허락조건하에서만 배포할 수 있습니다.

- 귀하는, 이 저작물의 재이용이나 배포의 경우, 이 저작물에 적용된 이용허락조건을 명확하게 나타내어야 합니다.
- 저작권자로부터 별도의 허가를 받으면 이러한 조건들은 적용되지 않습니다.

저작권법에 따른 이용자의 권리는 위의 내용에 의하여 영향을 받지 않습니다.

이것은 [이용허락규약\(Legal Code\)](#)을 이해하기 쉽게 요약한 것입니다.

[Disclaimer](#)

Finite Element Simulation of the Hard Turning Process with Patterned Tool Inserts



Dong Min Kim

Mechanical Engineering Program
Graduate school of UNIST

2013

Finite Element Simulation of the Hard Turning Process with Patterned Tool Inserts

Dong Min Kim

Mechanical Engineering Program
Graduate School of UNIST

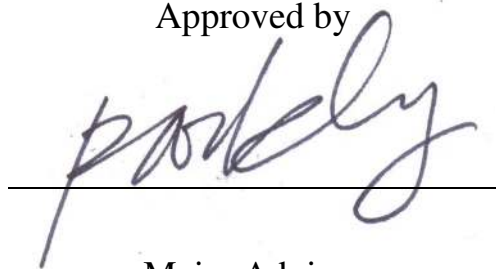
Finite Element Simulation of the Hard Turning Process with Patterned Tool Inserts

A thesis
submitted to the Graduate School of UNIST
in partial fulfillment of the
requirements for the degree of
Master of Science

Dong Min Kim

02. 18. 2013.

Approved by

A handwritten signature in black ink, appearing to read 'park', is written over a horizontal line. The signature is stylized and cursive.

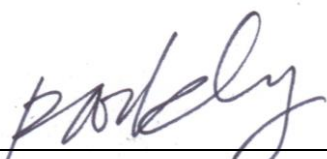
Major Advisor
Dr. Hyung Wook Park

Finite Element Simulation of the Hard Turning Process with Patterned Tool Inserts

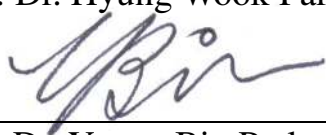
Dong Min Kim

This certifies that the thesis of Dong Min Kim is approved.

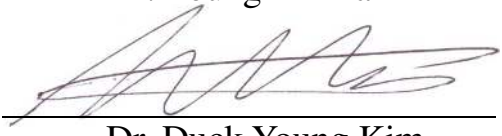
02. 18. 2013



Thesis Supervisor: Dr. Hyung Wook Park



Dr. Young Bin Park



Dr. Duck Young Kim

SUMMARY

Hard turning is a process for fabricating precise components from hardened steels using diamond-like tool materials such as cubic boron nitride. The main characteristic of hard turning is the dry machining process, which introduces challenges such as high friction and temperature that decrease the production rate. Research has been used to address these issues through approaches such as textured surfaces and textured tools to reduce the friction coefficient. However, the use of the finite element method (FEM) with textured machine tools has not been investigated until now.

This study proposes reducing the friction of the tool–chip interface using a textured tool rake surface. The technique was modeled in simulations using the DEFORM software package. The data for the workpiece and tool material for the simulations were based on FEM machining research. The initial results of the simulations were compared to theoretical modeling and experimental data. Four texture patterns were investigated: flat (non-patterned), perpendicular, parallel, and rectangular. In addition, the effects of the edge distance, pitch size, pattern height, and shear friction factors were also considered.

Of the four pattern types, the tool with the perpendicular pattern was best at reducing the force. An edge distance of 100 μm also tended to reduce the force. A pitch size of 100 μm and a pattern height of 50 μm produced the lowest force values for a perpendicular pattern. Furthermore, a shear friction factor of 0.6 gave reasonable results for all patterns. The lowest ratios for the cutting force/feed force and the cutting force/thrust force did not occur under conditions that resulted in the lowest force; it was a linear function of the pitch size and friction constants. The effective stress on the workpiece was widely distributed on the chip for the lower cutting forces, and the chip rotated in the direction of the pattern. Furthermore, the flow angle increased proportionally to the cutting force.

Overall, the texture pattern had an effect on the force; a tool with a perpendicular texture resulted in the least force. The coefficient of friction was not directly proportional to the force. The different forces affected the effective stress of the workpiece, and the pattern type and size affected the chip flow angle.

Future work will address the need for real experiments with textured tools so that experimental and simulated results can be compared. The cutting conditions will be changed by adjusting the cutting speed, feed rate, and depth of cut.

CONTENTS

1. INTRODUCTION	1
1.1 Hard turning with textured tools	1
1.2 Research objectives and approach	3
1.3 Dissertation organization	4
2. LITERATURE REVIEW	5
2.1 Fundamentals of hard turning modeling	5
2.1.1 Cutting mechanism modeling in hard turning	5
2.1.2 Thermal effect modeling in hard turning	9
2.2 FEM for cutting metal	10
2.2.1 FEM formulation	10
2.2.2 The damage theory for chip separation	12
2.2.3 Friction and Heat Transfer	13
2.3 Textured Inserts	15
3. FINITE ELEMENT MODELING OF TEXTURED TOOLS	18
3.1 Introduction	18
3.2 Textured geometry modeling on the tool surface	18
3.3 Workpiece modeling with flow stress data for AISI52100	22
3.4 Boundary condition	24
3.5 Comparison between simulation and experiments	25
3.6 Summary	26
4. PREDICTION OF TEXTURE GEOMETRY EFFECTS ON THE TOOL SURFACE	27
4.1 Texture shape	27
4.2 Edge distance	30
4.3 Pitch and height	34
4.4 Friction factor	37
4.5 Thermal effect and waviness on the chip	42
4.6 Summary	44

5. CONCLUSIONS AND RECOMMENDATIONS 45

5.1 Summary of work 45

5.2 Conclusions 45

5.3 Recommendations for future work 46

LIST OF FIGURE

Fig. 1-1. Comparison of conventional machining and hard turning (Dogra et al., 2010).	1
Fig. 1-2. Production cost of end surface finishing on a hardened gear (Hasan, 1998).	1
Fig. 1-3. 80- μm micro-dimpling pattern (left) and frictional properties for a patterned surface (right) (Wakuda et al., 2003).	3
Fig. 2-1. Cutting models: (a) The orthogonal and (b) oblique.	6
Fig. 2-2. (a) Shear plane model and (b) The slip line field model.	7
Fig. 2-3. Three heat sources in metal cutting, including tool wear (Huang and Liang, 2003).	9
Fig. 2-4. (a) Lagrangian, (b) Eulerian, and (c) ALE formulations.	11
Fig. 2-5. Geometrical Separation (Mamalis et al., 2001).	12
Fig. 2-6. Distribution of (a) normal stress and (b) shear stress on the cutting edge (Zhou et al., 2003).	14
Fig. 2-7. Curves representing the stresses distributions on the rake face (Zorev, 1963).	14
Fig. 2-8. Charge-coupled device micrographs of four types of micro-texture coated with DLC for groove and pit widths of $w = 50 \mu\text{m}$: (a) perpendicular; (b) parallel; (c) pit, and (d) dot. (Obikawa et al., 2011).	15
Fig. 2-9. Scanning electron microscopy images of a cutting tool with a (a) microtexture (pitch of $10 \mu\text{m}$) and (b) nanotexture (pitch of 800 nm) patterned by a femtosecond laser. Cross-sectional trace of the (c) microtexture and (d) nanotexture measured with an atomic force microscope (Kawasegi et al., 2009).	16
Fig. 2-10. (a) Cutting tools with nano-/micro-textured surface (b) Cutting tool with micro-textured surface (Sugihara and Enomoto, 2009).	16
Fig. 2-11. (a) Micro-grinding of a micro-groove array on tool rake surface (b) Dry turning using a micro-grooved tool (Xie et al., 2012).	17
Fig. 3-1. Tool geometry used in the simulations and transferred in STL file format.	19
Fig. 3-2. Textured tool CAD models used in the simulations.	21
Fig. 3-3. Local domain portion of the workpiece analysis in DEFORM.	23
Fig. 3-4. Flow-stress of AISI52100 (62 HRC) according to (Huang, 2002) equation.	23
Fig. 3-5. Mesh modeling for the FEM.	24
Fig. 3-6. Comparison of predicted and measured forces in the (a) cutting and (b) feed directions during cutting tests (Al-Zkeri, 2007).	25

Fig. 3-7. Comparison of predicted and experimental data.	25
Fig. 4-1. (a) Quasi-steady-state area of cutting force depending on texture pattern and (b) predictive force of various texture shapes.	28
Fig. 4-2. (a)–(d) Effective stress on the tool–workpiece cross-section; (e)–(h) chip flow angle.	31
Fig. 4-3. (Fig. 4-3. (a) Quasi-steady-state area of the cutting force as a function of edge distance, and (b) predictive force and ratios (cutting force/feed force, cutting force/thrust force) for the perpendicular and parallel textures for edge distances of 100 and 150 μm . The effective stress of the workpiece cross-section on (c) a perpendicular tool with no edge and (d) a parallel tool with an edge distance of 150 μm	31
Fig. 4-4. (a) Predictive force and ratios (cutting force/feed force, cutting force/thrust force) for the perpendicular pattern as a function of edge distance. (b)–(e) Effective stress of the workpiece cross-section on a perpendicular tool as a function of the edge distance.	32
Fig. 4-5. Chip flow angle at edge distances of (a) 50 μm , (b) 100 μm , (c) 150 μm , and (d) 300 μm	33
Fig. 4-6. (a) Effect of pitch size on the predictive force and ratios (cutting force/feed force, cutting force/thrust force). (b)–(d) Effective stress of the workpiece cross-section on a perpendicular tool as a function of pitch size. (e)–(g) Chip flow angle as a function of pitch size.	35
Fig. 4-7. (a) Effect of height on the predictive force and ratios (cutting force/feed force, cutting force/thrust force). (b), (c) Effective stress of the workpiece cross-section on a perpendicular tool as a function of height. (d), (e) Chip flow angle as a function of height.	36
Fig. 4-8. Predictive force and ratios (cutting force/feed force, cutting force/thrust force) (a) flat and (b) perpendicular texture patterns.	38
Fig. 4-9. Predictive force and ratios (cutting force/feed force, cutting force/thrust force) (a) parallel and (b) rectangular texture patterns.	39
Fig. 4-10. Chip morphology and stress distribution for the (a)–(c) flat and (d)–(f) perpendicular textures.	40
Fig. 4-11. Chip morphology and stress distribution for the (a)–(c) parallel and (d)–(f) rectangular textures.	41
Fig. 4-12. (a) Predictive temperature and ratios (cutting force/feed force, cutting force/thrust force) for the (b) flat, (c) perpendicular, (d) parallel, and (e) rectangular textures.	42
Fig. 4-13. Scanning electron microscopy images of chips generated while turning aluminum alloy under dry conditions showing (a) a nanotextured tool with perpendicular waviness and (b) an enlarged image of (a), and (c) a nanotextured tool with parallel waviness and (d, e) enlarged images indicated by A and B (Kawasegi et al., 2009). (f) Effective stress on the chip for the perpendicular texture. .	43

LIST OF TABLES

Table 3-1. Tool Geometry Specification used in the simulations(Dawson, 2002).	18
Table 3-2. Low CBN tool material properties.	19
Table 3-3. Thermal conductivity and heat capacity as functions of temperature (Heath, 1987, Ng et al., 1999).	20
Table 3-4. Simulation parameters related to tool geometry.	20

1. INTRODUCTION

1.1 Hard turning with textured tools

Hard turning is a machining process that increases productivity by improving the material removal ratio in hardened steel (50–70 HRC) using high speed and a single-point contact method. Hard turning typically uses cutting tools made of cubic boron nitride (CBN), ceramics, and cermet (Konig, 1984). CBN in particular is quite diamond-like in its characteristics and exhibits good wear resistance. CBN tools are formed by sintering CBN particles with cobalt, TiC, TiN, and other materials. In general, there are two varieties of CBN materials: those with high CBN content (90%) and those with low CBN content (50%–70%) (Zhang, 2005a).

Hard turning has particular advantages when manufacturing engines, bearings, and precision components with levels of roughness as low as Ra 100–500 nm without machine grinding. Traditional machining processes require many steps to produce finished products (Fig. 1-1). The grinding process is followed by surface finishing in conventional machining, which increases both cost and machining time (Fig. 1-2). The rate of material removal is higher in hard turning than in conventional machining.

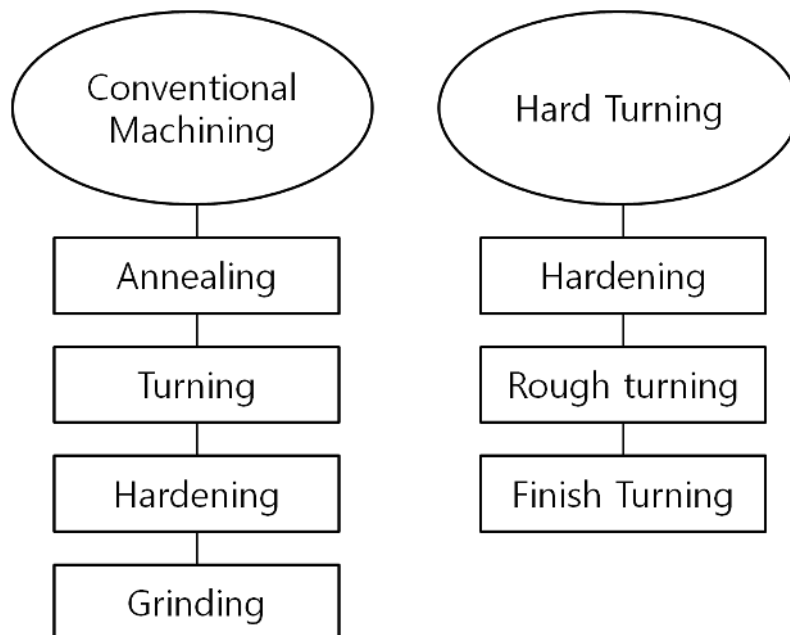


Fig. 1-1. Comparison of conventional machining and hard turning (Dogra et al., 2010).

The hard turning process is characterized by dry machining, which means not using cutting fluid to reduce the temperature between the tool and the workpiece to achieve good surface quality. Even so, the surface roughness in hard turning is similar to the finish achieved in conventional grinding machining, although the temperature can reach 900°C or more. Because the white layer generated on the surface of the workpiece increases its surface roughness, research is underway to find ways of reducing the temperature.

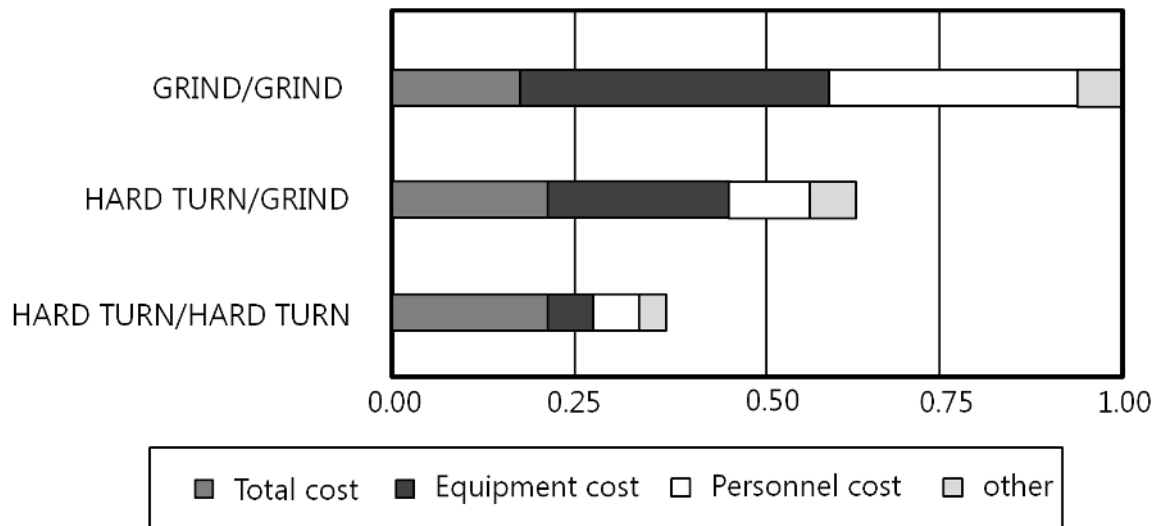


Fig. 1-2. Production cost of end surface finishing on a hardened gear (Hasan, 1998).

However, hard turning does have certain limitations (Al-Zkeri, 2005) that need to be addressed before it can replace grinding machining in industrial applications. These limitations include the following:

- shortage of machining database expertise,
- a resulting surface roughness of 0.2 μm, and
- the tool that wear quickly and have a short life, increasing the production time for large components.

The biggest problem in the hard-turning process is high friction, which decreases tool life and increases tool wear because of high temperature. This leads to increased cycle time and cost. Therefore, reducing the friction between the tool and the workpiece is extremely important in improving the hard-turning process. Two approaches are generally used. The more popular is to use a liquid lubricant, such as oil or grease, through the minimum quantity lubrication (MQL) approach. The less popular way is to use a textured surface to improve tribological characteristics (Bruzzone et al., 2008).

The effect of a textured surface on friction is dependent on the texture pattern (Bruzzone et al., 2008, Evans and Bryan, 1999). Research has shown that the cutting force and friction coefficient are reduced by appropriate selection of the texture geometry (Jianxin et al., 2012, Kawasegi et al., 2009). Cutting tools are generally made of carbide (WC-Co) or have a diamond-like carbon (DLC) coating (Obikawa et al., 2011), while workpiece materials are aluminum or Ti-6Al-4V. Most previous research has been conducted without the benefit of computer simulation. However, (Jianxin et al., 2012) examined dry cutting with a textured rake face on carbide tools, and showed the effect of the von Mises stress and cutting force on textured tools using the finite element (FE) method (FEM) with ANSYS software.

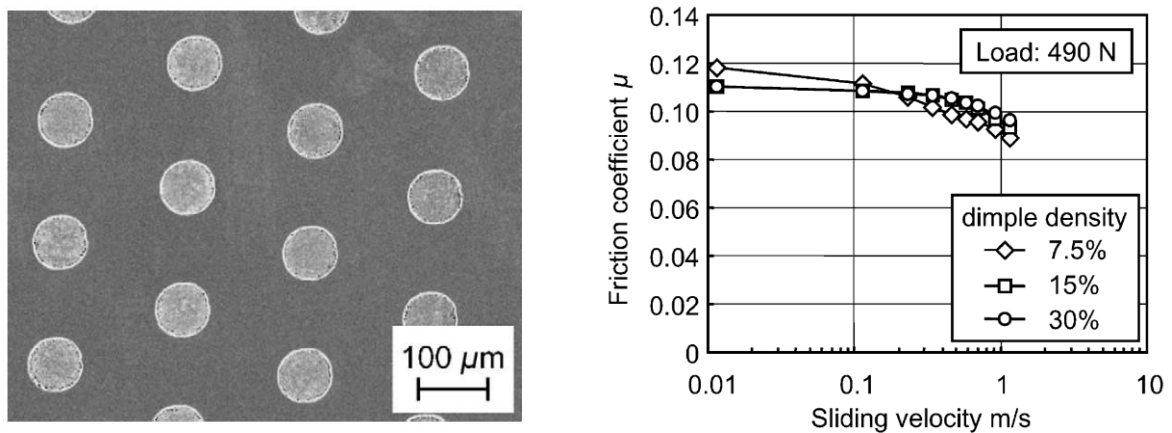


Fig. 1-3. 80- μm micro-dimpling pattern (left) and frictional properties for a patterned surface (right) (Wakuda et al., 2003).

1.2 Research objectives and approach

The goal of this research is to use the FEM to analyze the hard-turning process with a textured tool and predict the effects of the texture geometry (pattern shape) as well as the texture size, distance to the cutting force, and temperature. The detailed objectives are the following:

- Compare the theory of hard-turning modeling to a FEM database, which has structured data from Johnson–Cook (J–C) modeling, along with experimental data from a literature review,
- Study the effect of tool geometry on the surface related to the texture pattern, size, edge distance to the cutting force, temperature, strain, stress, and chip direction using FEM modeling, and
- Find the coefficient of calculation for patterned insert simulation, which has coincided with in-situ data.

This research took place in three steps.

- Step 1: Develop a material database for FEM from J–C modeling using AISI52100 steel workpiece with CBN tools.
- Step 2: Determine which geometric factors (e.g., texture pattern and size) reduce friction.
- Step 3: Compare the results for stress, temperature, strain, and strain rate to experimental data and primary FE analysis in other papers.

1.3 Dissertation organization

SECTION 1. INTRODUCTION

This section outlines the hard-turning process, and briefly describes the effect of surface texture. This section also describes the research objectives, approaches, and organization of each section.

SECTION 2. LITERATURE REVIEW

This section includes the theory of the fundamental metal cutting mechanism in the hard-turning process, including Oxely's theory of two- and three-dimensional (2D and 3D) turning, and the effect of temperature, strain, and stress. This section also describes the FEM formulation for basic metal cutting, including meshing, criteria, and the way of used.

SECTION 3. FINITE ELEMENT MODELING OF TEXTURED TOOLS

This chapter discusses the boundary conditions of textured tool FEM in terms of workpiece (AISI52100)/tool (CBN) property data, formulation, friction, mesh design, and cutting condition parameters.

SECTION 4. PREDICTION OF TEXTURE GEOMERY EFFECTS ON THE TOOL SURFACE

This chapter presents the results of texture geometry effects and compares the texture parameters.

SECTION 5. CONCLUSIONS AND RECOMMENDATIONS

This section presents conclusions and recommendations for future research.

2. LITERATURE REVIEW

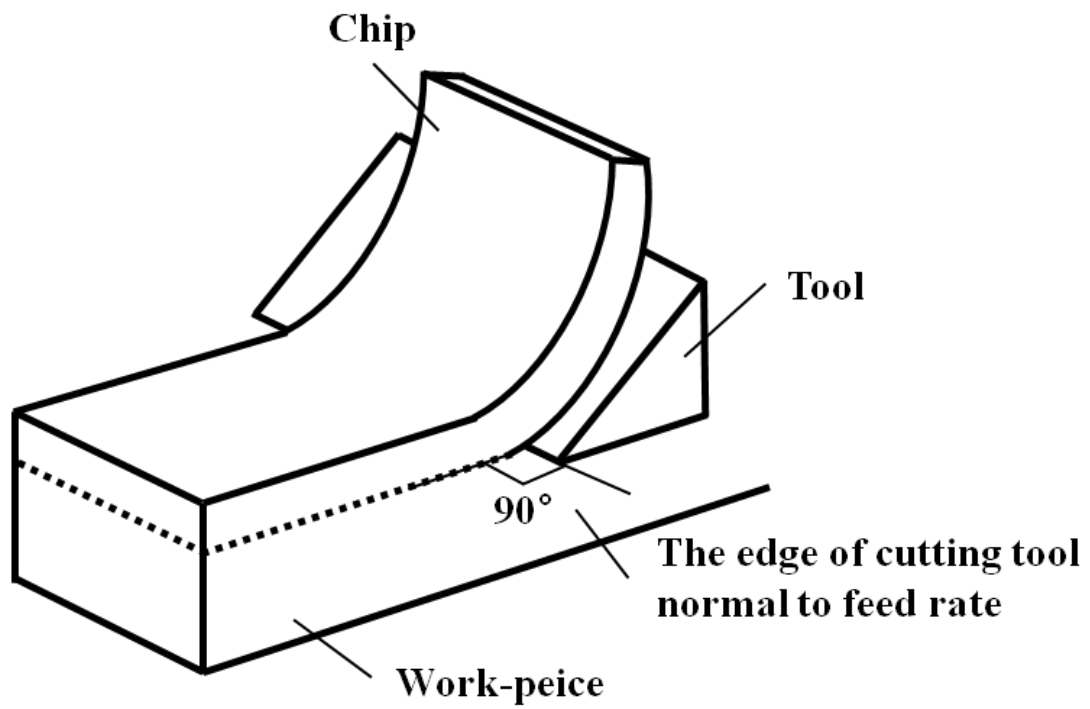
2.1 Fundamentals of hard-turning modeling

Machining is a material removal process in which unnecessary material from the workpiece is removed in the form of chips. Machining processes include turning, milling, drilling, sawing, broaching, shaping, and grinding are classified as either single-point or multipoint cutting processes. Turning uses a lathe to modify the surface of a cylinder or cone. The surface quality is determined by several factors, including the workpiece, cutting tools, and machine tool. Machining operations will not be efficient or economic without a fundamental understanding of the interrelationships of these factors. Thus, understanding the modeling for force and thermal effects is very important.

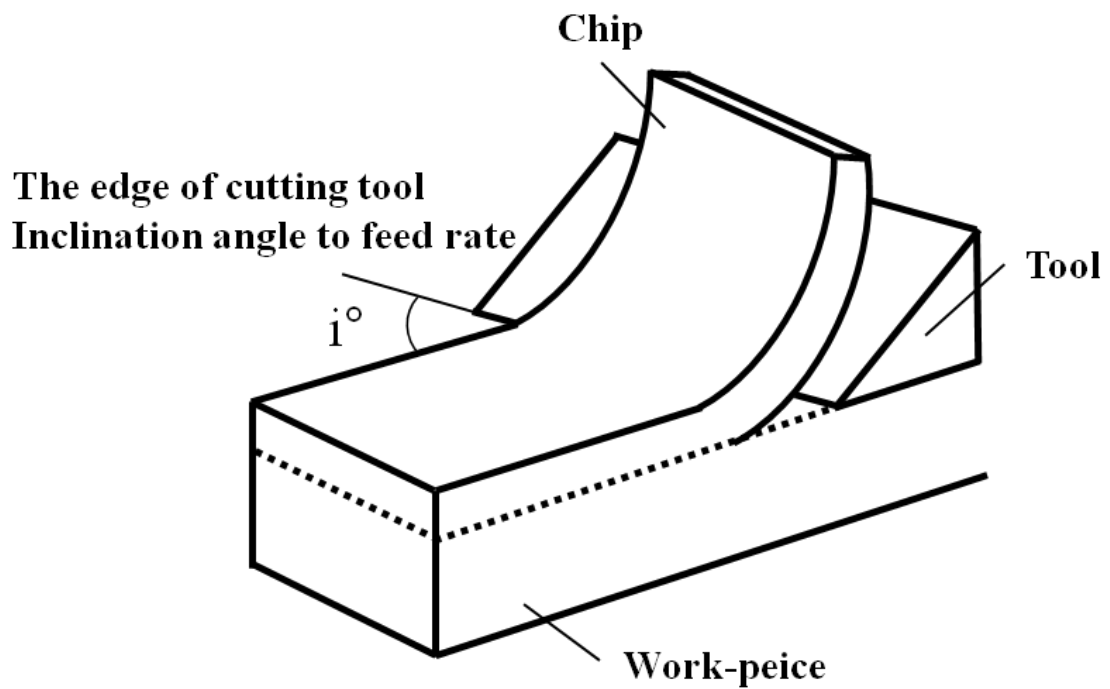
2.1.1 Cutting mechanism modeling in hard turning

Fundamental research into cutting mechanics involves two theoretical approaches: orthogonal and oblique machining processes. In the orthogonal cutting model, the edge of the cutting tool is normal to the feed direction, as shown in Fig. 2-1(a). The orthogonal cutting model is used in 2D machining. However, in this model, the deformation zones for chip formation are only considered in plane-strain deformation with no transversal force component. The oblique cutting model is used in 3D turning machining, in which the edge of the cutting tool is at an angle of less than 90° to the feed direction. Most machining operations are actually 3D (Fig. 2-1(b)).

The cutting force is related to the mechanics of chip formation, which has been examined from two perspectives: the minimum energy principle and the slip line field theory. The minimum energy is generated in the shear plane following the direction of the shear angle (Merchant, 1945) (Fig. 2-2(a)). The slip line theory considers the strain, strain-rate, and flow stress. The chip is formed in the direction of the slip line due to plasticity.

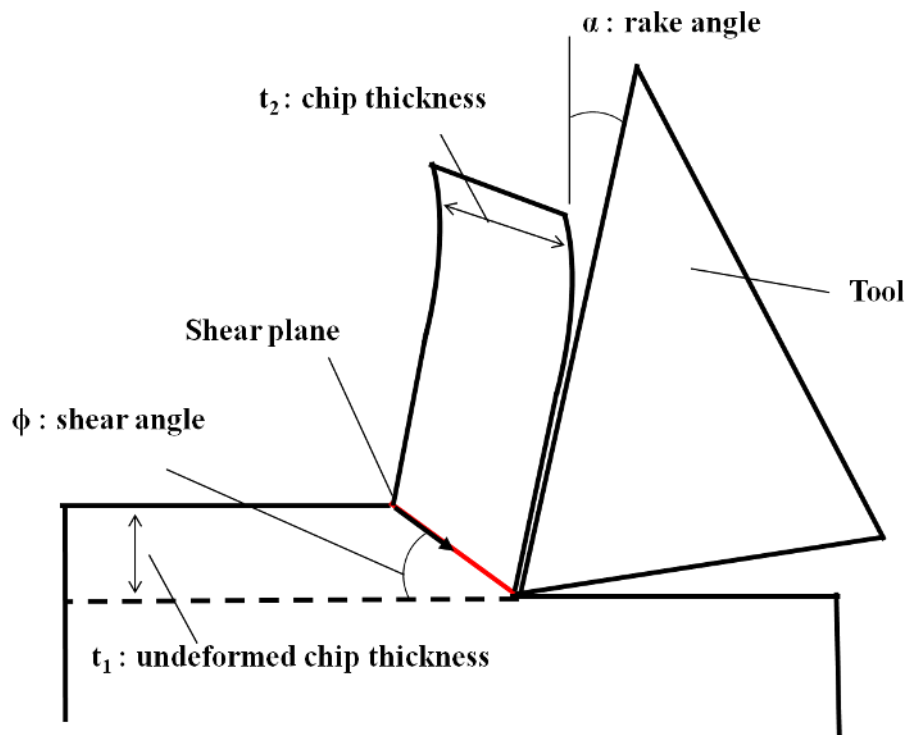


(a)

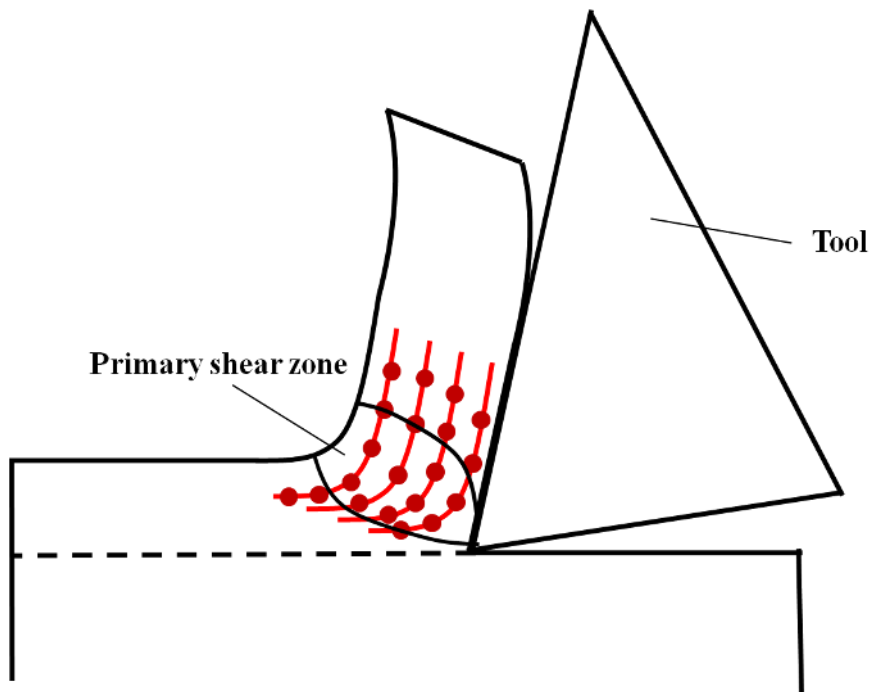


(b)

Fig. 2-1. Cutting models: (a) The orthogonal and (b) oblique.



(a)



(b)

Fig. 2-2. (a) Shear plane model and (b) The slip line field model.

The cutting forces in hard turning have three components: chip formation, plowing, and sliding. Zhang (Zhang, 2005b) considered the sum of forces due to chip formation and tool wear for 3D oblique forces in the hard-turning process. However, we considered only a fresh tool in our experiments.

The forces due to chip formation are the cutting force P_c , the axial force P_a , and the radial force P_r , as shown in Eq. (2-1).

$$P_c = F_C, \quad P_a = F_Q \cos C_s^* + F_r \sin C_s^*, \quad P_r = F_Q \sin C_s^* - F_r \cos C_s^* \quad (2-1)$$

Where:

$$F_r = \frac{F_C (\sin i^* - \cos i^* \sin \alpha_n^* \tan \eta_c^*) - F_Q \cos \alpha_n^* \tan \eta_c^*}{\sin i^* \sin \alpha_n^* \tan \eta_c^* + \cos i^*} \quad (2-2)$$

The cutting edge normal rake angle α_n^* , the inclination angle i^* , and the side cutting edge angle C_s^* from 3D oblique cutting geometry can be transformed to 2D cutting geometry. The chip flow angle can be determined using Stabler's flow rule (Stabler, 1951), as shown in Eq. (2-6). Thus, the cut width ω^* and the undeformed chip thickness t^* are determined using Eq. (2-7).

$$i^* = \sin^{-1}(\cos \eta_o \sin i - \sin \eta_o \sin \alpha_n \cos i) \quad (2-3)$$

$$\alpha_n^* = \sin^{-1} \left(\frac{\sec \eta_o \sin i - \sin i^*}{\tan \eta_o \cos i^*} \right) \quad (2-4)$$

$$C_s^* = C_s + \eta_o \quad (2-5)$$

$$\eta_c^* = i^* \quad (2-6)$$

$$t^* = f \cos C_s^*, \quad \omega^* = d / \cos C_s^* \quad (2-7)$$

The turning force is due to shear force, which is related to the workpiece material equation. The Johnson–Cook equation (Johnson and Cook, 1983) is used as the constitutive model of the workpiece (Eq. 2-8).

$$\sigma = \left(A + B \varepsilon^n \right) \left(1 + C \ln \frac{\dot{\varepsilon}}{\dot{\varepsilon}_o} \right) \left(1 - \left(\frac{T - T_r}{T_m - T_r} \right)^m \right) \quad (2-8)$$

This model is a function of the strain ϵ , strain-rate $\dot{\epsilon}$, temperature T , and five constants (A , B , C , m , and n). If the temperature increases, the material will become softer, and the strain and strain rate will change.

2.1.2 Thermal effect modeling in hard turning

Hard turning is a type of dry machining; it uses no cutting fluid. The temperature can quickly rise to a high level. Because high temperatures affect machined parts, understanding this heat generation process is important. Figure 2-3 shows three heat sources: the primary heat source from the shear zone, the secondary heat source from the friction zone, and the rubbing heat source from the interface between the workpiece and the tool. While the primary heat source generates heat along the shear plane, almost all of this heat diffuses to the workpiece and the chip. The rubbing heat source is particularly significant for machining using worn tools.

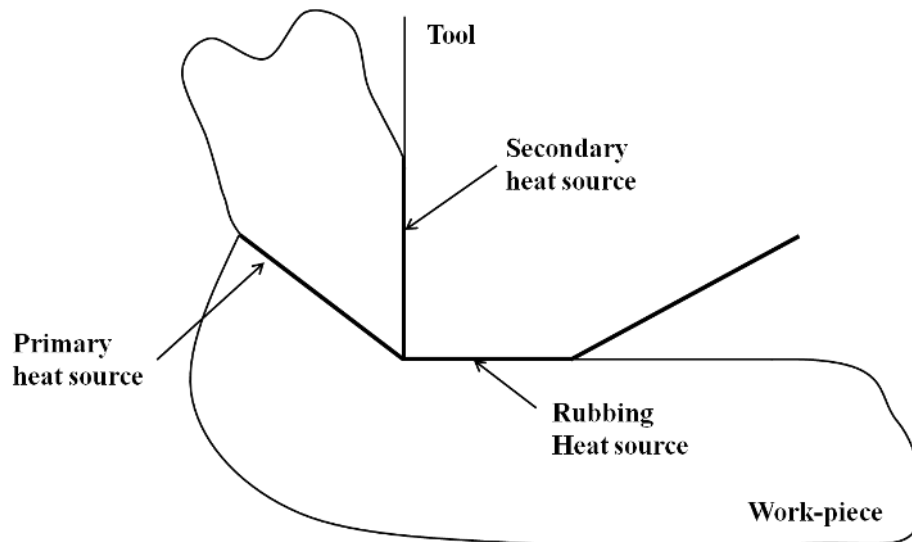


Fig. 2-3. Three heat sources in metal cutting, including tool wear (Huang and Liang, 2003).

Boothroyd(Boothroyd, 1963) and Oxley(Oxley, 1989) proposed average temperature rake face \bar{T}_{ra} .(Eq. 2-9)

$$\bar{T}_{ra} = T_o + \Delta T_{SZ} + \psi \Delta T_M + \Delta T_{VB} \quad (2-9)$$

Where ΔT_{SZ} is the temperature contributed by the primary heat source, ΔT_C is the temperature contributed by the secondary heat source in the chip, ΔT_M is the maximum temperature from the secondary heat source in the chip, and ΔT_{VB} is the temperature from the rubbing heat source.

$$\Delta T_{SZ} = \frac{(1-\beta)F_S V_S}{\rho C V_C a^* t^*} \quad (2-10)$$

$$\Delta T_C = \frac{FV_{chip}}{\rho C V_C a^* t^*}, \quad \ln\left(\frac{\Delta T_M}{\Delta T_C}\right) = 0.06 - 0.195\delta\left(\frac{R_T t_2}{h}\right)^{1/2} + 0.5\ln\left(\frac{R_T t_2}{h}\right) \quad (2-11)$$

$$\Delta T_{VB} = \frac{\Gamma F_{CW} V_c}{\rho C V_C a^* t^*} \quad (2-12)$$

2.2 FEM for cutting metal

Research into metal cutting has been mainly experimental. Although FE simulation modeling has been used (KOMVOPOULOS et al., 1991, MacGinley and Monaghan, 2001, Özel, 2006), the complexity of the cutting process has extremely limited its application. Because any single FEM approach cannot be applied to all cutting processes, understanding cutting FEM algorithm principles is important. This chapter discusses previous work that has applied FEM to cutting.

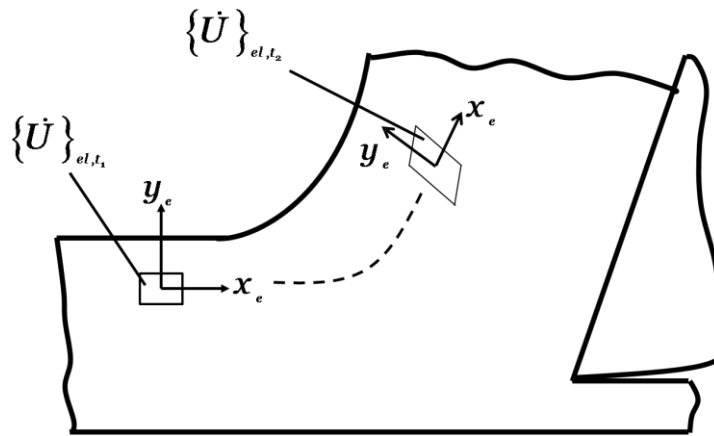
2.2.1 FEM formulation

There are three approaches to FE formulation based on continuum mechanics: Lagrangian, Eulerian, and arbitrary Lagrangian Eulerian (ALE).

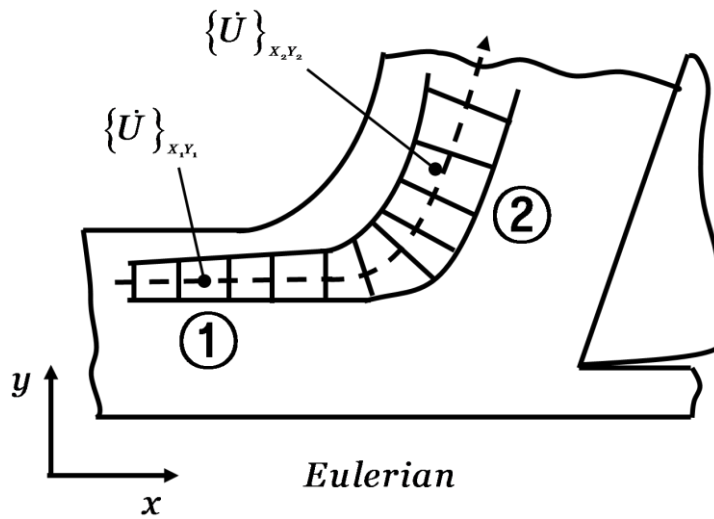
The Lagrangian formation involves moving the reference frame, as shown in Fig. 2-4(a) (Childs, 2000), which requires a chip separation criterion. The mesh elements change shape to replace the distorted element by remeshing (Komvopoulos and Erpenbeck, 1991, Ueda and Manabe, 1993, Zhang and Bagchi, 1994, Özel, 2006). The Lagrangian formulation has the advantage of predicting chip formation.

The Eulerian formulation does not require a chip separation criterion at steady state. The advantage of the Eulerian formulation is its short computation time. It also requires fewer mesh elements than the Lagrangian formation, and, as shown in Fig. 2-4(b), requires no distorted mesh (Carroll Iii and Strenkowski, 1988, STENKOWSKI et al., 1990, Childs and Maekawa, 1990, Childs, 2000). However, this formulation is unsuitable for actual metal cutting processes.

The ALE approach, shown in Fig. 2-4(c) (Özel, 2006), is a formulation that combines the advantages of the Lagrangian and Eulerian formulations, and is used in commercial software packages such as DEFORM and Abaqus/Explicit. The tool mesh is fixed while the material reference frame is moved in the cutting direction, as in the Lagrangian formation. The chip flow is analyzed in the same manner as in the Eulerian formation.



Lagrangian



Eulerian

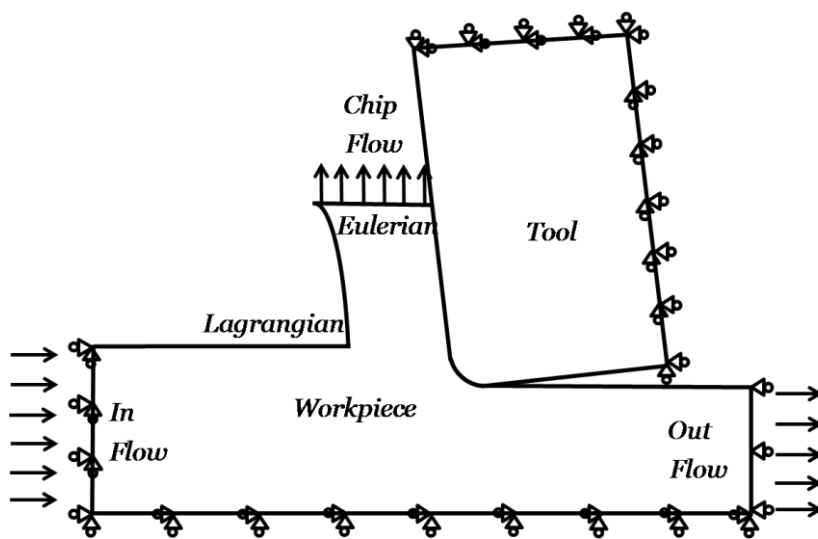


Fig. 2-4. (a) Lagrangian, (b) Eulerian, and (c) ALE formulations.

2.2.2 The damage theory for chip separation

Chip separation is implemented as a fracture criterion in the DEFORM program. Ductile fracturing reaches the point of plastic strain, as expressed in Eq. (2-13) (McClintock, 1968).

$$\int_0^{\bar{\epsilon}_f} f(\text{stress state}) d\bar{\epsilon} = C \quad (2-13)$$

where f is a weighting function, $\bar{\epsilon}$ is the equivalent strain, $\bar{\epsilon}_f$ is the equivalent strain to fracture, and C is a material constant.

When the tool mesh has the same mesh as the workpiece, the chip is generated at the point of fracture (Eq. 2-13). As shown in Fig. 2-5(a), there are two categories for graphical chip separation. In the first category, a predefined line exists to the cut depth. When the cutting tool edge and element distance become less than the critical distance D_c , node E can be separated into new components E and E' . This process is conducted sequentially until the chip has been formed. The other method is continuous remeshing based on large plastic deformation.

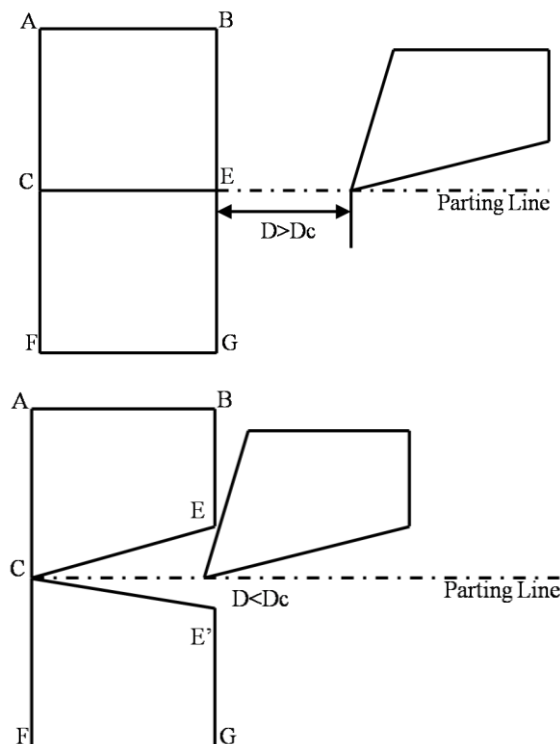


Fig. 2-5. Geometrical Separation (Mamalis et al., 2001).

2.2.3 Friction and Heat Transfer

Friction conditions are complex and can be characterized in various ways. Friction depends on the cutting condition, tool edge geometry, and other factors (Childs, 1998). The numerical process of friction in FE models has been assumed to fall into two categories.

The first category is the Coulomb model,

$$\mu = \frac{\tau}{\sigma_N} \quad (2-14)$$

where μ is the coefficient of friction, τ is the frictional stress, and σ_N is the normal stress. Figure 2-6(a) shows the normal stress distributed on the tool edge. In the DEFORM program, the frictional stress is calculated using the flow stress of the workpiece (SFTC, 2008). For hard turning, some researchers have assumed a value of 0.3–0.35 for the coefficient of friction (GUO et al., 2002, Ramesh et al., 2005).

The second category is the shear model,

$$\tau = m \cdot K_{chip} \quad (2-15)$$

where τ is the frictional shear stress, K_{chip} is the shear yield stress, and m is the friction factor. A value of $m = 0$ indicates a frictionless interface, while a value of $m = 1$ indicates a sticking friction interface. This friction is used mostly for bulk-forming simulations. Several researchers have assumed a shear friction coefficient of $m = 0.5$ (Umbrello et al., 2004, Mamalis et al., 2002). (Zorev, 1963) assumed that the tool edge had two friction regions, as shown in Fig. 2-7.

The sticking region is applied to the constant shear stress along with l_p , the length of the sticking region, where $l_p = 2\text{feed}$. The sliding region then respects Coulomb's law because the shear stress decreases following the rake face.

The friction due to plastic deformation at the tool–chip interface generates heat (Subbiah, 2006). The heat transfer is assumed to result in heat conduction only in the workpiece material. The governing equation of this heat transfer is

$$K \frac{\partial^2 T}{\partial x^2} + K \frac{\partial^2 T}{\partial y^2} = \rho_m C_p \left(u \frac{\partial T}{\partial y} + v \frac{\partial T}{\partial x} \right) + \dot{Q} \quad (2-16)$$

where K is the thermal conductivity of the workpiece, ρ_m is the mass density, C_p is the specific heat capacity, u is the velocity in the x -direction, v is the velocity in the y -direction, and \dot{Q} is the volume heat flux. The tool–chip heat transfer coefficient was assumed to be $28 \text{ N/s/mm/}^\circ\text{C}$ for the FE analysis (Umbrello et al., 2004).

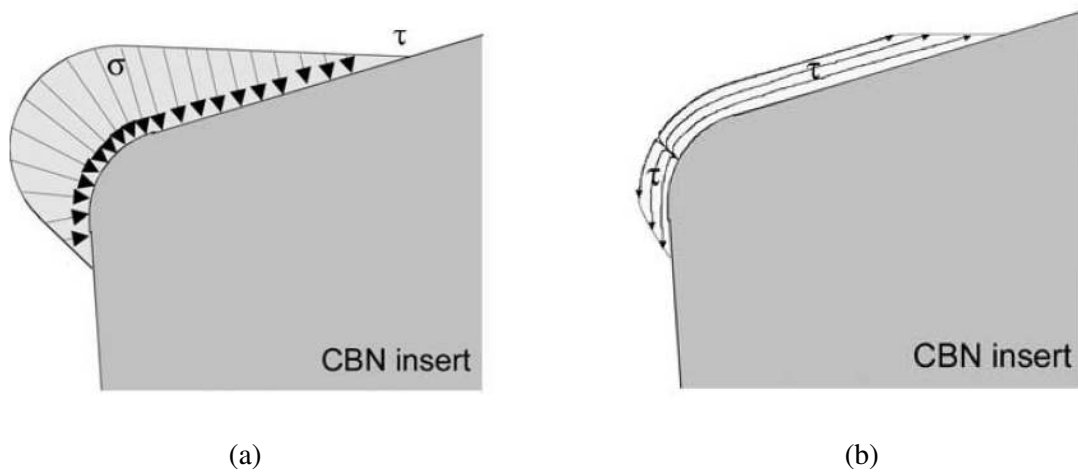


Fig. 2-6. Distribution of (a) normal stress and (b) shear stress on the cutting edge (Zhou et al., 2003).

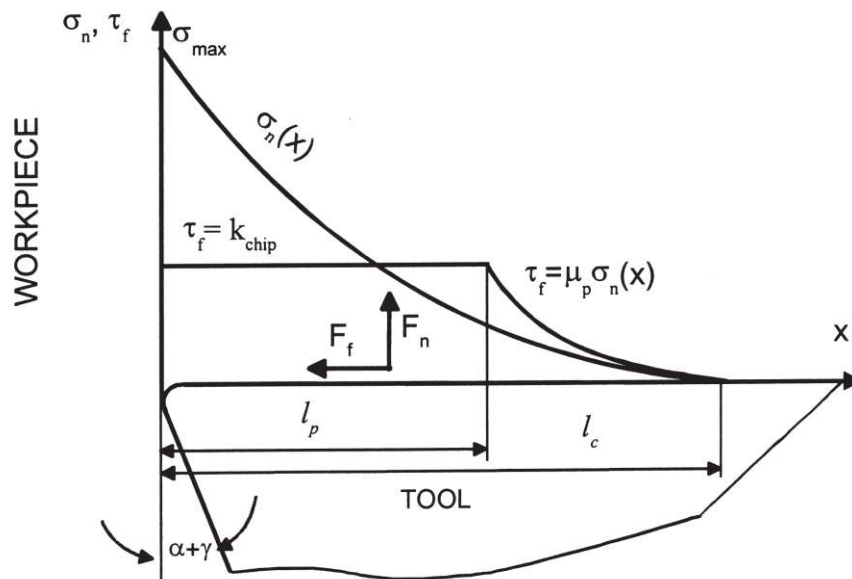


Fig. 2-7. Curves representing the stresses distributions on the rake face (Zorev, 1963).

2.3 Textured Inserts

A textured surface reduces friction and improves lubrication (Bruzzone et al., 2008), but only if the texture is less than micro-sized (Pettersson and Jacobson, 2006). Larger texture sizes (e.g., macro-sized) increase friction. Smaller texture sizes reduce friction because the debris from wear becomes entrapped in the texture geometry (Pettersson and Jacobson, 2006, Dubrujeaud et al., 1994) and lubrication is better (Blatter et al., 1999, Costa and Hutchings, 2009, Erdemir, 2005).

Textured surfaces can be applied to various regions in optical, mechanical contact, hydrodynamics, metrology artifacts, friction and wear, adhesion, thermal, and machining applications. (Tatsumi et al., 1999) developed the single crystal diamond engineered tool shown in Fig. 2-8, which has a texture size of 2–3 mm in macro units. This tool had a high removal rate and increased active grit number. (Hintze W., 1998) also developed a textured tool for material removal machining that reduced friction. It had reduced contact length and increased tool life.

Surface engineering technologies have been developed that add or remove material. For machining tool applications, the adding material process involves coating the tool surface with a DLC. (Obikawa et al., 2011) fabricated coated tools with micro-textured surfaces (Fig. 2-8) using four geometric patterns: perpendicular, parallel, pits, and dots.

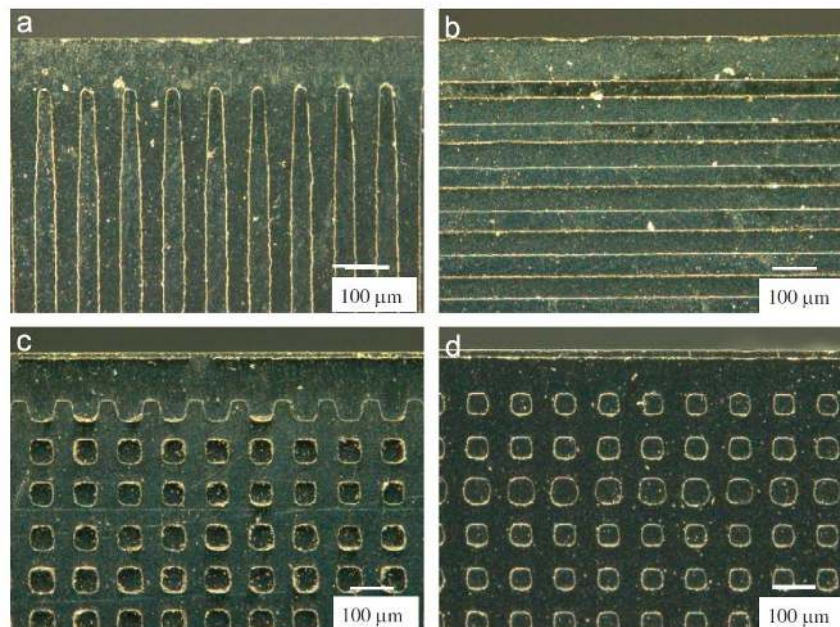


Fig. 2-8. Charge-coupled device micrographs of four types of micro-texture coated with DLC for groove and pit widths of $w = 50 \mu\text{m}$: (a) perpendicular; (b) parallel; (c) pit, and (d) dot (Obikawa et al., 2011).

Manufacturing methods for material removal to produce textured tools include laser machining, grinding machining, and electrical discharge machining. In laser machining, the texture pattern is fabricated through the ablation and interference phenomena of a femtosecond laser (Kawasegi et al., 2009, Sugihara and Enomoto, 2009). Kawasegi and Sugihara have developed textured tools for turning machining (Fig. 2-9) and milling machining (Fig. 2-10), and have researched the effect of micro-textured and nano-textured tools.

For grinding machining, the grinding wheel has a V-tip applied by a dresser, as shown in Fig. 2-11(a). The micro-texture on the tool rake surface is arrayed by the grinding wheel, as shown in Fig. 2-11(b). Experimental results have indicated that a micro-grooved tool may reduce cutting sparks, the tool–chip contact length, and tool wear (Xie et al., 2012).

The results of previous research have shown micro-size patterning effectively reduces the friction force, coefficient of friction, and contact length. Smaller pattern sizes and deeper textures contribute to a lower friction factor.

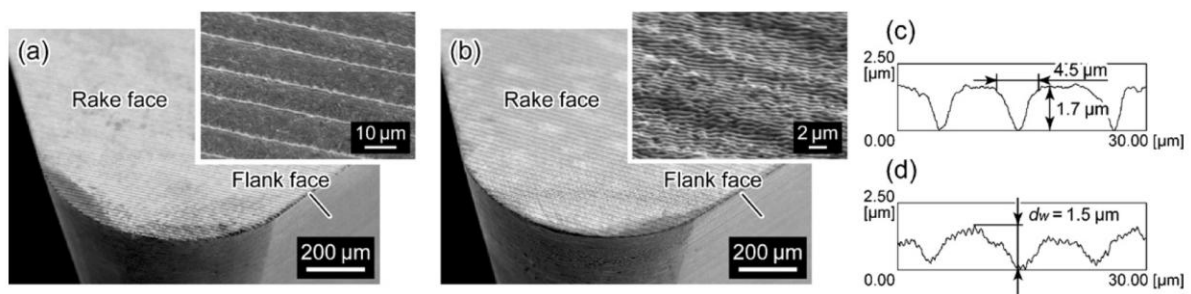


Fig. 2-9. Scanning electron microscopy images of a cutting tool with a (a) microtexture (pitch of 10 μm) and (b) nanotexture (pitch of 800 nm) patterned by a femtosecond laser. Cross-sectional trace of the (c) microtexture and (d) nanotexture measured with an atomic force microscope (Kawasegi et al., 2009).

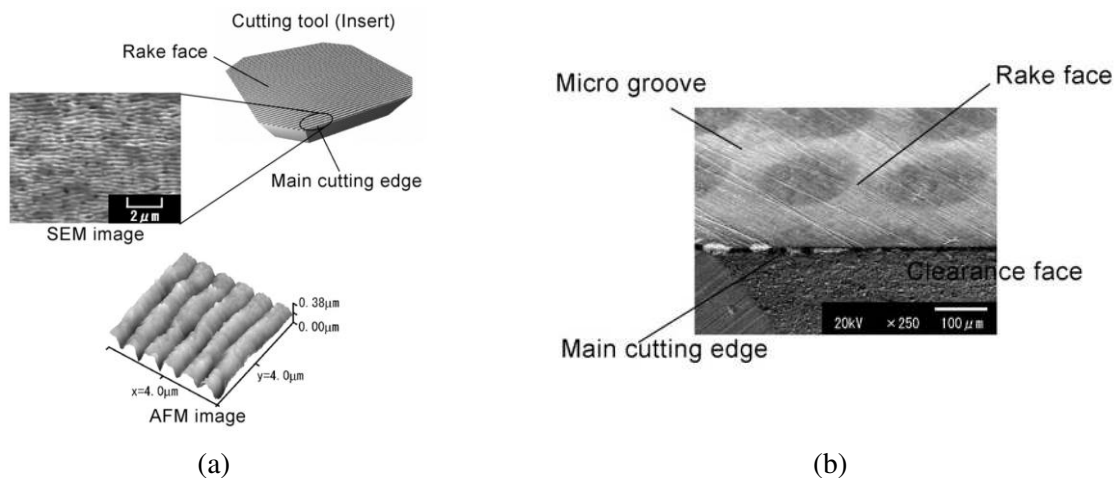


Fig. 2-10. (a) Cutting tools with nano-/micro-textured surface (b) Cutting tool with micro-textured surface (Sugihara and Enomoto, 2009).

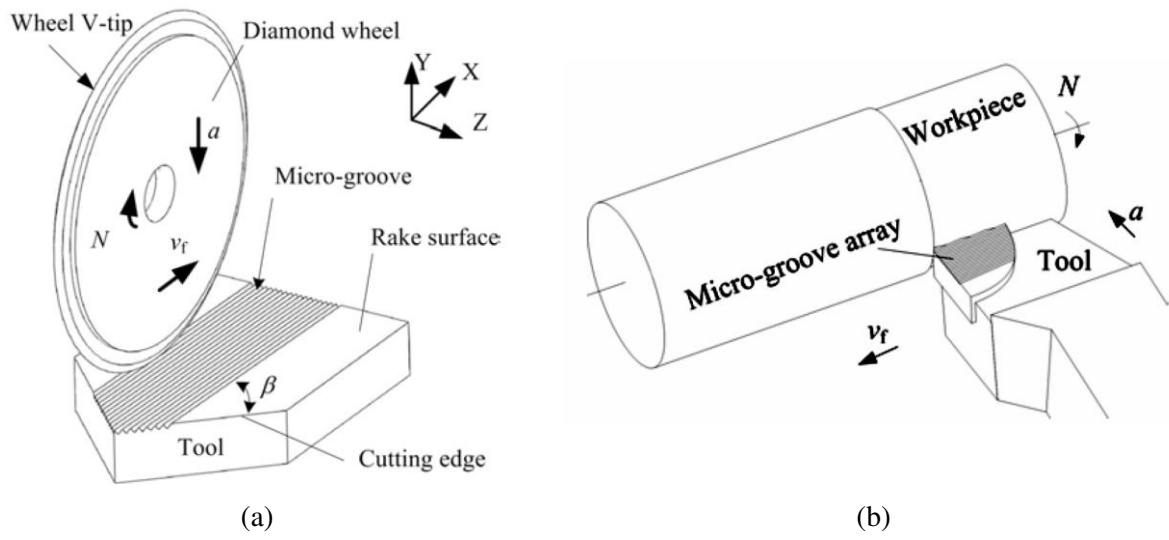


Fig. 2-11. (a) Micro-grinding of a micro-groove array on tool rake surface (b) Dry turning using a micro-grooved tool (Xie et al., 2012).

3. FINITE ELEMENT MODELING OF TEXTURED TOOLS

3.1 Introduction

This chapter describes the complete details of FEM for hard turning using texture geometries with patterns taken from previous research. The FE analysis follows details of the boundary conditions, such as friction, as well as mesh control details and data related to the tools and materials. Experimental and FEM data from the literature are compared with the results of previous simulations. All of the simulations consisted of 3D FEM.

3.2 Textured geometry modeling on the tool surface

The tool geometry (Table 3-1) was the same as that used by (Dawson, 2002) to allow comparison between our experimental data and other FEM data.

The modeling geometry was first drawn using Solidworks 2012, and then the geometry files were exported in stereolithography (STL) file format for transfer to DEFORM-3D. The nose radius was 0.8 mm with no assumed chamfer or hone. The geometry used in the simulations was part of the tool tip (black portion in Fig. 3-1(a), shown in greater detail in Fig. 3-1(b)). The tip size was 2 mm from the edge of the tool, which was the CBN-brazed section of a real tool. Figure 3-1(b) shows the pattern on the surface of the tools. The edge distance is one of the parameters that affects the force or machineability (Obikawa et al., 2011). Figure 3-1(d) shows the STL format of the model in DEFORM.

The analytic modeling of the tool was done in rigid mode. Table 3-2 shows the properties of the tool material. The data can be found in various sources in the literature. There are two categories of CBN content: low (50%–70%) and high (greater than 90%) (Al-Zkeri, 2007). These simulations considered only low CBN.

Table 3-1. Tool Geometry Specification used in the simulations(Dawson, 2002).

Tool Geometry Specification	Value
Nose radius, r_n	0.8 mm
Side Rake Angle, γ_0	-5°
Back Rake Angle, χ_s	-5°
Side Cutting Angle, λ_c	-5°

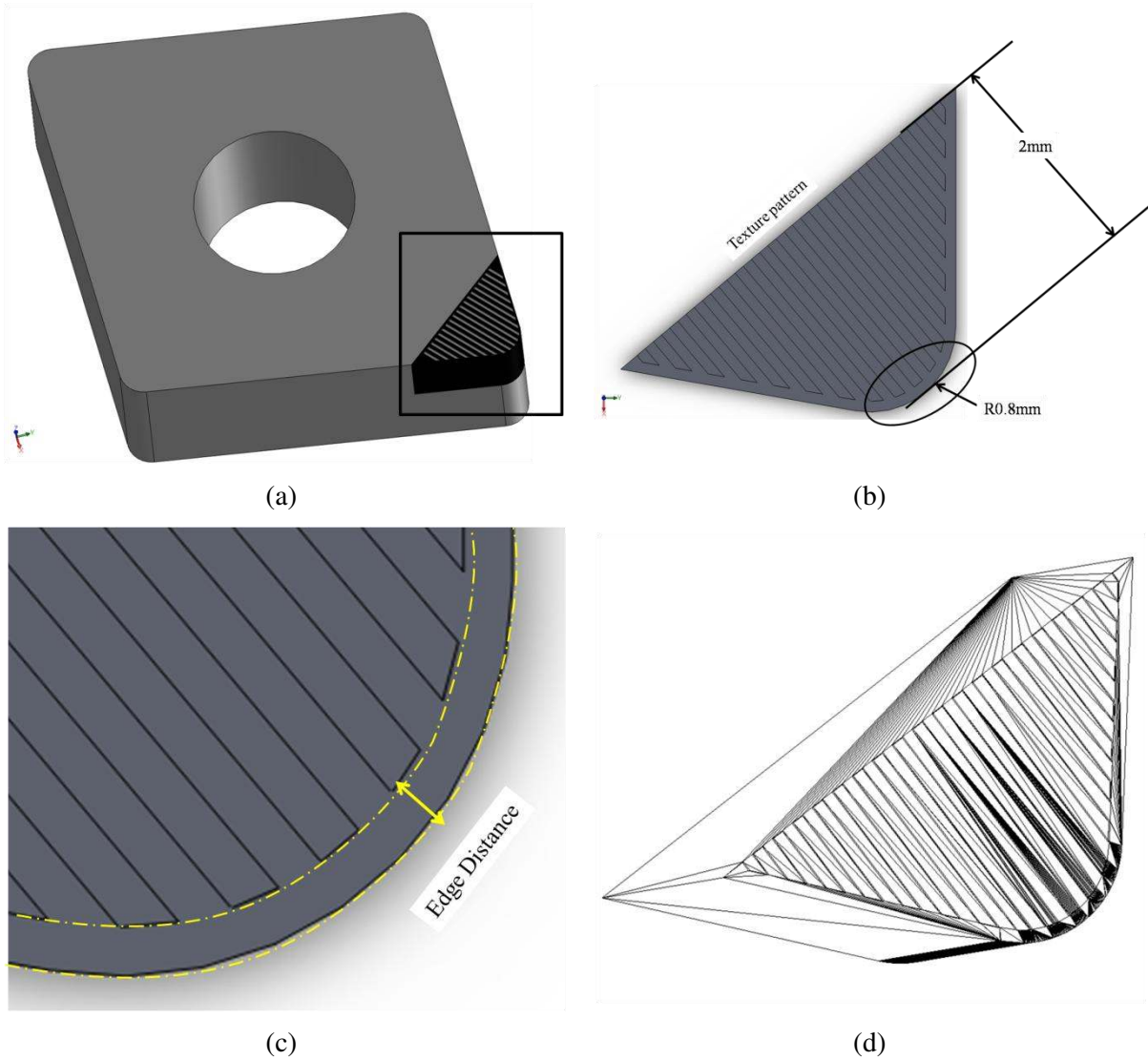


Fig. 3-1. Tool geometry used in the simulations and transferred in STL file format.

Table 3-2. Low CBN tool material properties.

Properties	Value	Reference
Young's Modulus (GPa)	588	(Ng et al., 1999)
Poisson's ratio	0.17	
Thermal expansion($\times 10^{-6}/^{\circ}\text{C}$)	0.47	(Heath, 1987)
Emissivity	0.45	(Ng et al., 1999)
Thermal Conductivity (N/sec/ $^{\circ}\text{C}$)	f(T)	(Heath, 1987)
Heat Capacity (N/mm $^2/^{\circ}\text{C}$)	f(T)	

Table 3-3. Thermal conductivity and heat capacity as functions of temperature (Heath, 1987, Ng et al., 1999).

Temperature(°C)	Thermal Conductivity (N/sec/°C)	Heat Capacity (N/mm ² /°C)
20	59.4	2.7390
100	64.4	3.3308
200	67.7	3.9502
400	68.8	4.6751
600	66.7	5.0880
800	63.9	5.2991
900	62.0	5.3541
1000	59.5	5.3771

The geometry parameters in this study were defined as the texture shape, edge distance, pitch size, and texture height, the values of which are given in Table 3-4. As shown in Fig. 3-2, the texture patterns were non-textured (flat), perpendicular, parallel, and rectangular. The non-textured type (no pattern on the tool surface) was included for the sake of comparison. The perpendicular pattern had horizontal grooves, and the parallel pattern had a vertical cutting edge. The rectangular pattern was both horizontal and vertical.

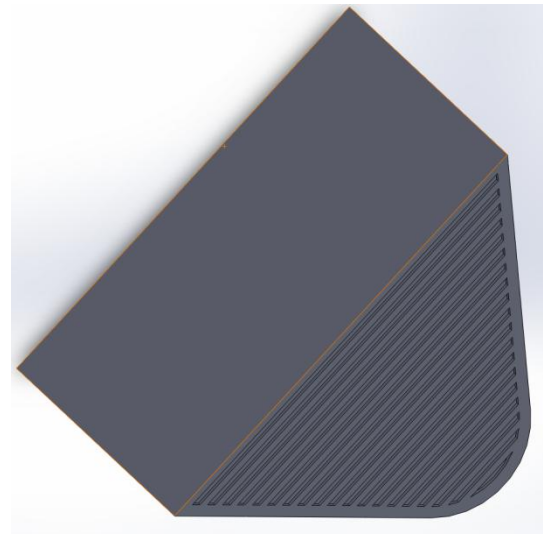
The edge distance is an important parameter due to the undeformed chip thickness of 100 μm (Obikawa et al., 2011). Thus, the effect of the edge distance was varied over the range 50–500 μm . In addition, the pitch and height of the texture were also varied. Table 3-4 lists the parameters considered.

Table 3-4. Simulation parameters related to tool geometry.

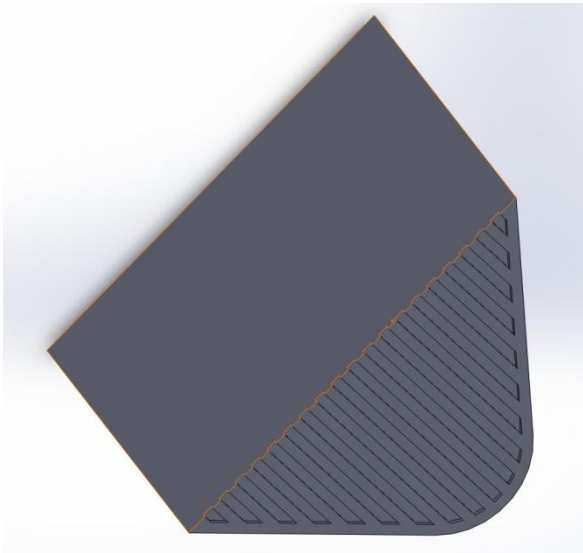
Parameter	Value
	Non-textured
texture shape	perpendicular
	parallel
	rectangular
edge distance (μm)	50/100/150/300/500
pitch size (μm)	50/100/150
texture height (μm)	50/100



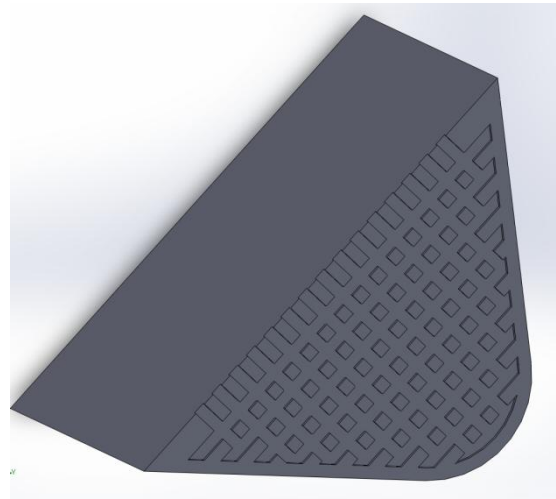
(a) flat(non-texture)



(b) perpendicular



(c) parallel



(d) rectangular

Fig. 3-2. Textured tool CAD models used in the simulations.

3.3 Workpiece modeling with flow stress data for AISI52100

The simulations assumed the use of AISI52100 bearing steel, 50 mm in diameter with a hardness of 62 HRC, as well as a local domain and a plastic mode. The workpiece model (Fig. 3-3) was designed in DEFORM considering the tool contact. The tool geometry was round, 5 mm in the cutting direction (y -direction), 0.66 mm high (z -direction), and 1.75 mm wide (x -direction). All workpiece models were the same, independent of the tool textures.

The Johnson–Cook flow-stress model, briefly introduced in Chapter 2 above, was judged to be suitable for the plastic behavior of AISI52100 (62 HRC) bearing steel. (Huang, 2002) examined the flow-stress of AISI52100 (62 HRC) bearing steel using orthogonal cutting experiments and force data. The force results were determined by minimizing the objective function given by Eq. (3-1). Equation (3-2) shows the results for the Johnson–Cook equation constant.

$$\min \left\{ \sqrt{\sum \left[(F_{c,SIM} - F_{c,EXP})^2 + w_t (F_{t,SIM} - F_{t,EXP})^2 \right]} \right\} \quad (3-1)$$

where $F_{c,SIM}$ is the cutting force, $F_{t,SIM}$ is the thrust force from the orthogonal cutting model, and w_t is a weight constant to compensate for any error that may be generated in the optimization process.

$$\bar{\sigma} = (774.78 + 134.46 \cdot \varepsilon^{0.3710}) \cdot (1 + 0.0173 \cdot \ln \dot{\varepsilon}) \cdot \left[1 - \left(\frac{T - 25}{1487 - 25} \right)^{3.1710} \right] MPa \quad (3-2)$$

where A (774.78 MPa) is the yield stress, B (134.46) is the strain hardening coefficient, n (0.3710) is the strain hardening exponent, C (0.0173) is the strain rate dependence coefficient, and m (3.1710) is the temperature dependence coefficient. The flow-stress(MPa) of AISI52100 is represented at 12 strain, 9 strain rate (s^{-1}), and 7 temperature($^{\circ}C$), as shown in Fig. 3-4.

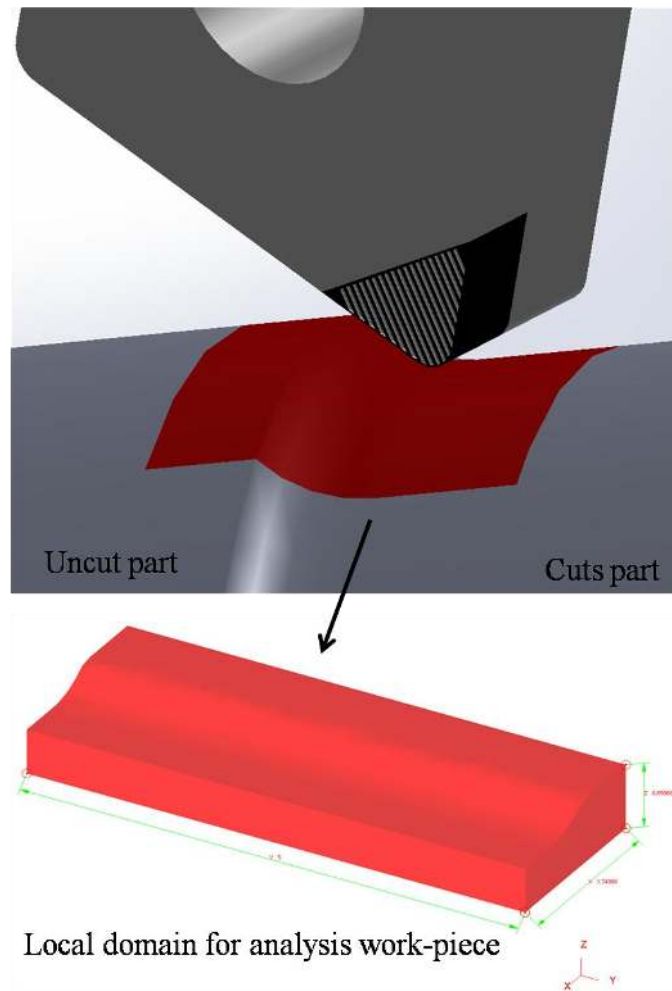


Fig. 3-3. Local domain portion of the workpiece analysis in DEFORM.

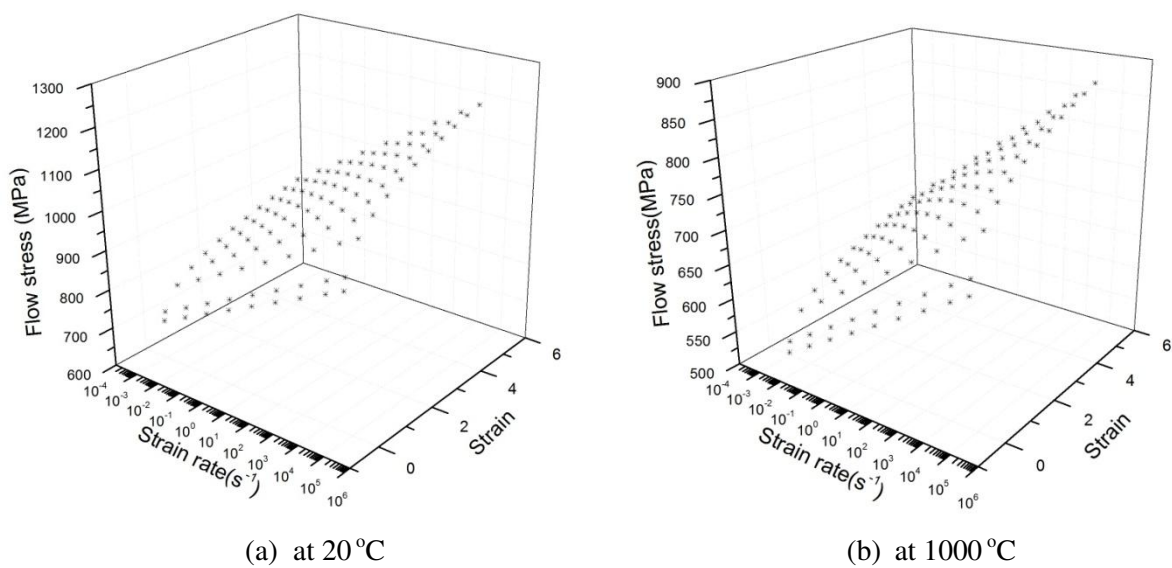
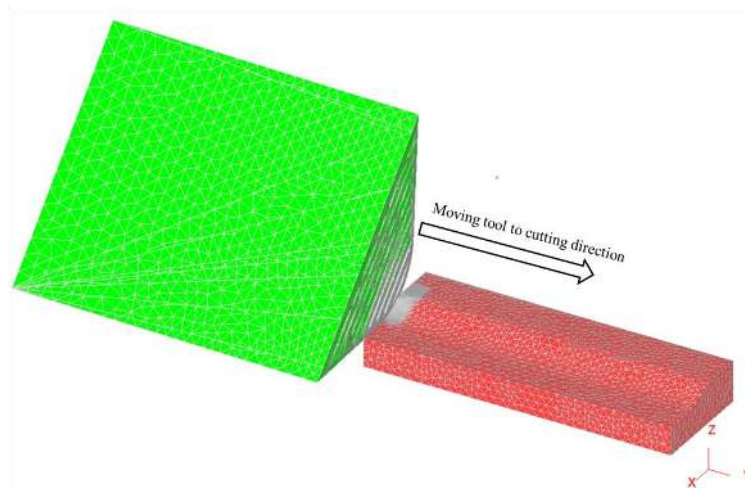


Fig. 3-4. Flow-stress(MPa) of AISI52100 (62 HRC) according to (Huang, 2002) equation.

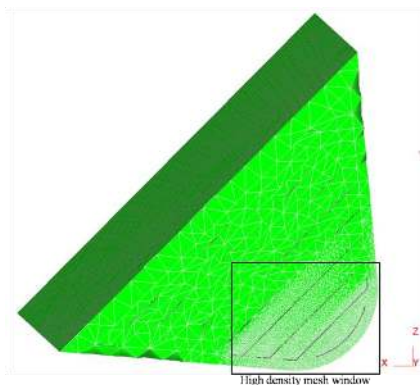
3.4 Boundary condition

The cutting conditions were fixed values taken from one of (Dawson, 2002) experiments: a cutting speed of 182.9 mm/min, a feed rate of 0.152 mm/rev, and a depth of cut of 0.203 mm. The environment was assumed to be room temperature (20°C), and the convection coefficient was assumed to be a constant 0.02 N/s/mm/°C. The tool–workpiece interface conditions were defined by the friction factor and the heat transfer coefficient. The friction was set to values of 0.2, 0.4, and 0.6 of constant shear friction while the heat transfer coefficient was a constant 28 N/s/mm/°C (Umbrello et al., 2004).

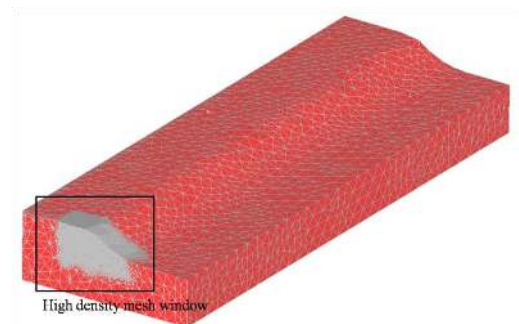
The finite element meshes of the tool and the workpiece were designed with a mesh window, as shown in Figs. 3-5(b) and 3-5(c). The meshes of the tool and the workpiece were limited to minimum element sizes of 0.02 and 0.015 mm, respectively. A tetrahedral mesh was used for both. The textured tool was moved in the cutting direction (y -direction) at a cutting speed of 182.9 mm/min. The feed direction (x -direction) and the thrust direction (z -direction) were determined.



(a) 3D FEM modeling



(b) textured tool



(c) workpiece

Fig. 3-5. Mesh modeling for the FEM.

3.5 Comparison between simulation and experiments

The results of the simulation are compared for one case of Dawson's experimental data in Fig. 3-7 using the cutting conditions shown in Fig. 3-4 with a fixed shear friction of 0.6). The following experimental data were compared: cutting force, feed force, and thrust force.

Slight differences were observed between the simulation and experimental data for the cutting force (11% difference) and feed force (5% difference). However, the difference between the thrust forces was much greater. (Al-Zkeri, 2007) discovered two reasons for this in 3D FEM (Fig. 3-6). First, the flow-stress did not cover the lower range of the strain, strain rate, and temperature. Second, the mesh was not small enough to predict the workpiece and tool tip behavior accurately.

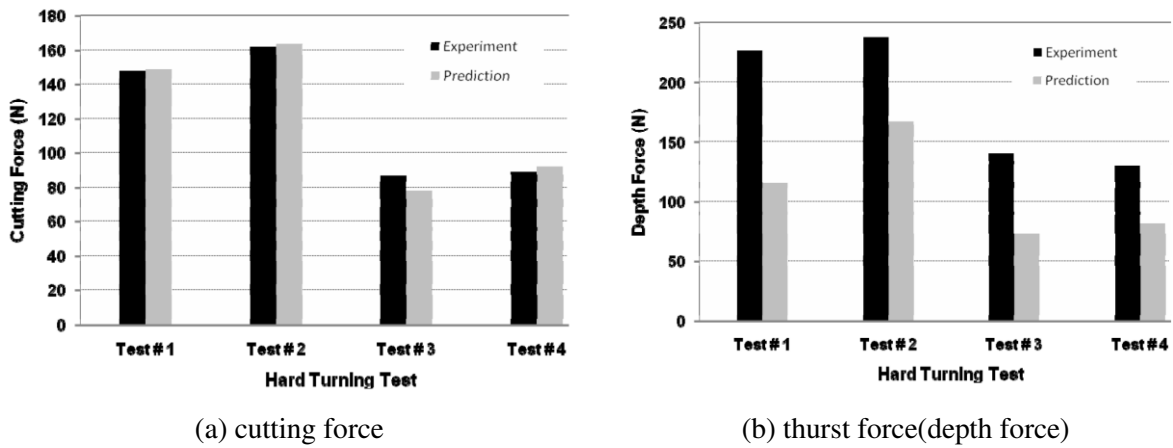


Fig. 3-6. Comparison of predicted and measured forces in the (a) cutting and (b) feed directions during cutting tests (Al-Zkeri, 2007).

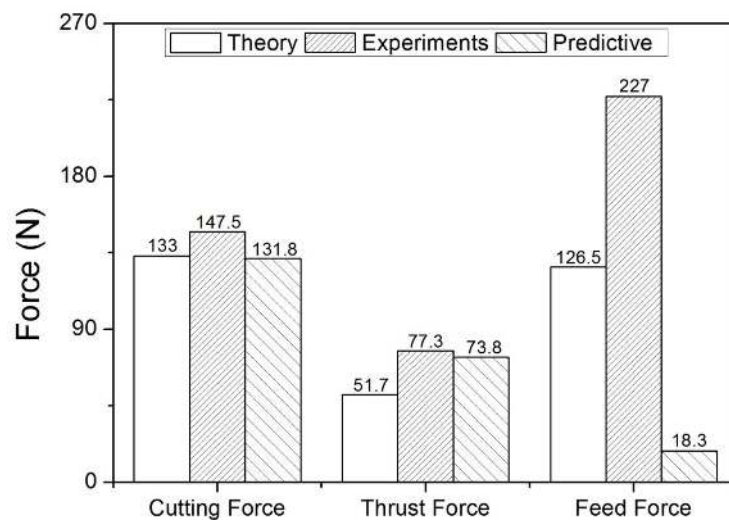


Fig. 3-7. Comparison of predicted and experimental data.

3.6 Summary

This chapter described the FEM conditions used for the DEFORM simulations. The tool was assumed to be of low-CBN, and four types of texture pattern were selected from previous research. The parameters related to the tool geometry were the edge distance, texture pattern, pitch size, and texture height. The workpiece was assumed to be made of AISI52100 (62 HRC) bearing steel. The flow-stress for AISI52100 was assumed to follow the Johnson–Cook equation. The meshes of the tool and workpiece were generated as high-density window meshes with minimum sizes of 0.02 and 0.01 mm, respectively. The friction parameter was set to 0.2, 0.4, and 0.6 of shear constant.

To validate the simulation conditions, the data were compared to Dawson's experimental data. The simulated and experimental values for the cutting force and feed force were in good agreement, but those for the thrust force were not. According to (Al-Zkeri, 2007), this was due to lack of small-scale strain, strain rate, and temperature results, as well as the lack of a sufficiently small mesh size.

4. PREDICTION OF TEXTURE GEOMETRY EFFECTS ON THE TOOL SURFACE

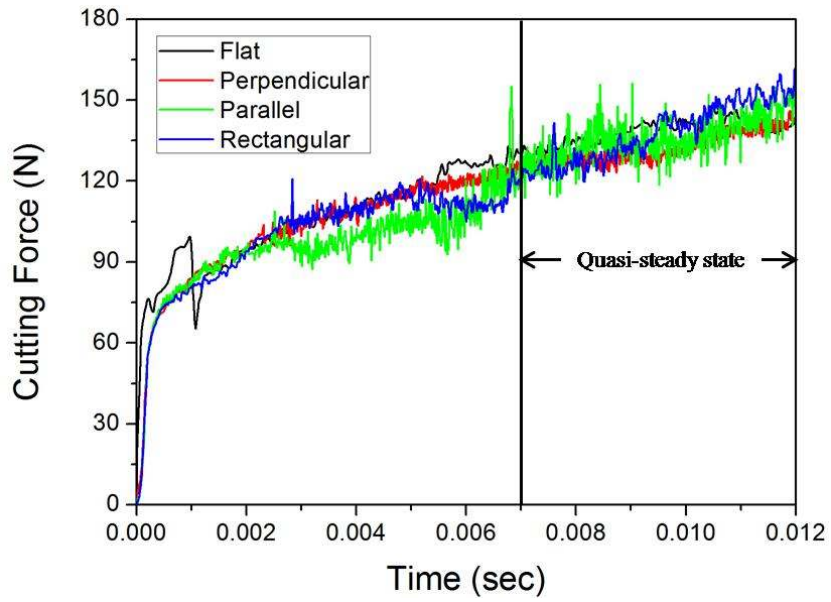
4.1 Texture shape

The four texture patterns were flat, perpendicular (+edge), parallel (+edge), and rectangular (+edge). The friction was fixed at a shear constant 0.6. The pitch size was 100 μm , the height was 50 μm , and the edge distance was 100 μm . Figure 4-1(a) shows the cutting force as a function of simulation time. The average calculation force data were taken from the quasi-steady-state area over the time period 0.007–0.012 s, as shown in Figure 4-1(b). Figure 4-1(b) had displayed standard deviation for fluctuation of the force in the quasi-steady-state area data.

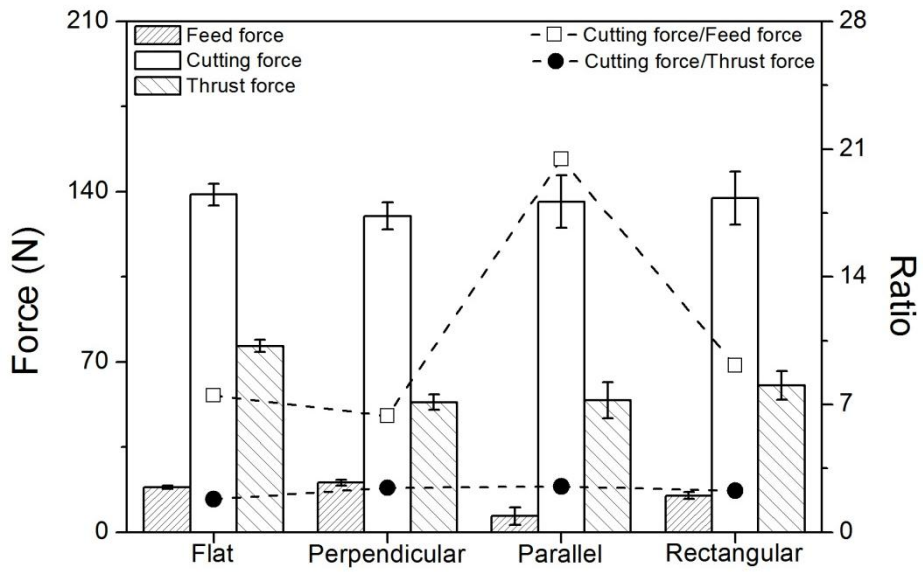
The feed force was similar for the flat and perpendicular-textured tools. The parallel-textured tool had the lowest feed force. Our results were somewhat different from than the experimental results (Kawasegi et al., 2009) where the perpendicular pattern had greater lower thrust and feed force than the parallel pattern did. The cutting force and thrust force were comparable for all tool texture types. The perpendicular-textured tool was best for reducing the cutting force, similar to the experimental results (Kawasegi et al., 2009, Obikawa et al., 2011).

The ratio for the cutting force/feed force were lowest for the perpendicular texture. The lowest cutting force occurred with the perpendicular texture. The largest ratio for the cutting force/feed force occurred for the parallel texture, as shown in Fig. 4-1(b). All of texture had similar to ratios of the cutting force/thrust force.

The chip was subject to more stress after the pitch position, as shown in Figs. 4-2(a)–(d). The parallel and rectangular textures clearly concentrated the stress on the pattern position. This pattern was interrupted following the chip, and the chip flow direction was determined by the pattern direction. The flat and rectangular textures had chip flow angles of 75°–76°. The perpendicular texture had the smallest chip flow angle (44°) following the pattern direction. The parallel texture had a 90° chip flow angle, which is why that chip was rotated in the parallel pattern direction. Thus, the perpendicular texture had the effect of decreasing the cutting force while the parallel and rectangular textures did not.

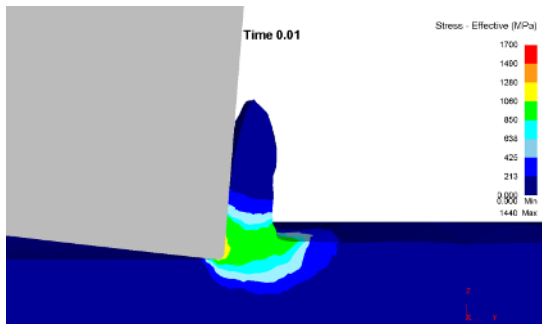


(a)

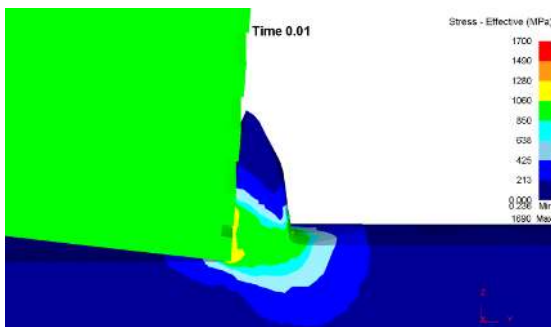


(b)

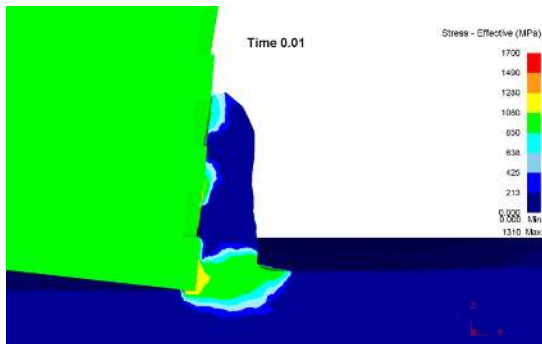
Fig. 4-1. (a) Quasi-steady-state area of cutting force depending on texture pattern and (b) predictive force of various texture shapes.



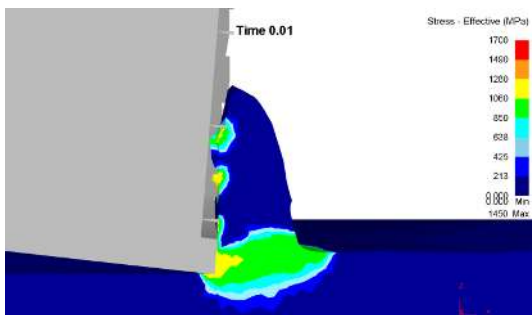
(a) flat



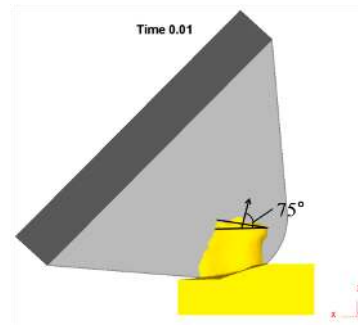
(b) perpendicular



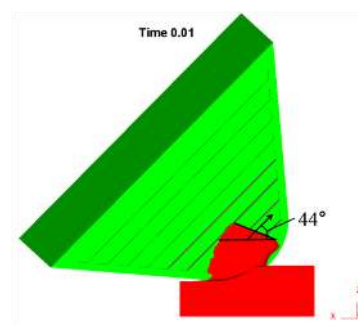
(c) parallel



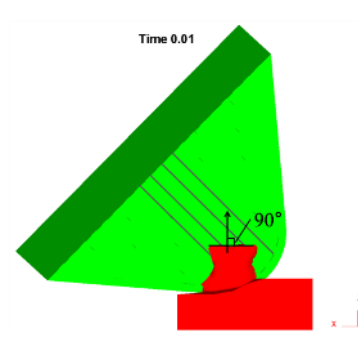
(d) rectangular



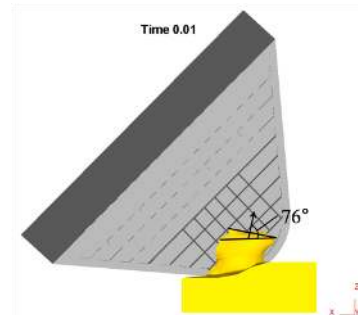
(e) flat



(f) perpendicular



(g) parallel



(h) rectangular

Fig. 4-2. (a)–(d) Effective stress on the tool–workpiece cross-section; (e)–(h) chip flow angle.

4.2 Edge distance

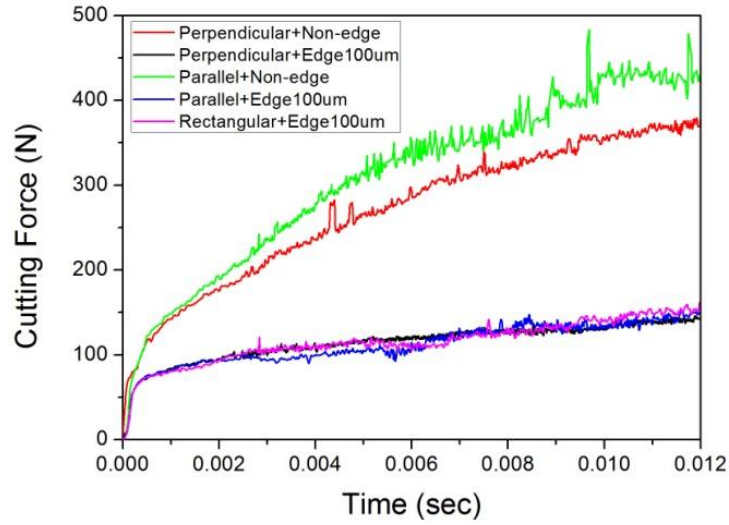
The results showed that a textured tool with no edge had higher force than one with an edge, and that this force increased with time. The force with a textured tool without an edge did not reach a steady state. A textured tool without an edge may fracture at the moment of contact with the workpiece because of the high force predicted by the simulation (Fig. 4-3 (a)). The tool edge is important to separate the chip from the workpiece when cutting metal. The cross-section of a non-edge perpendicular-texture simulation confirmed that the maximum stress was not in the shear zones, but rather distributed along the chip, which means that it did not affect cutting (Fig. 4-3 (c)).

The feed force with the perpendicular-textured tool decreased as the edge distance increased, while with the parallel pattern, the feed force increased as the edge distance increased. The cutting force and thrust force increased as the edge distance increased. The force for a parallel pattern with an edge distance of 150 μm was not concentrated in the shear zone (Fig. 4-3(d)) because the tool–chip contact zone on the rake face increased to the edge distance. In addition, the ratios increased for the perpendicular pattern and diminished for the parallel pattern. This does not agree with the experimental results of (Obikawa et al., 2011), who observed that the cutting force and thrust force decreased with the perpendicular pattern texture.

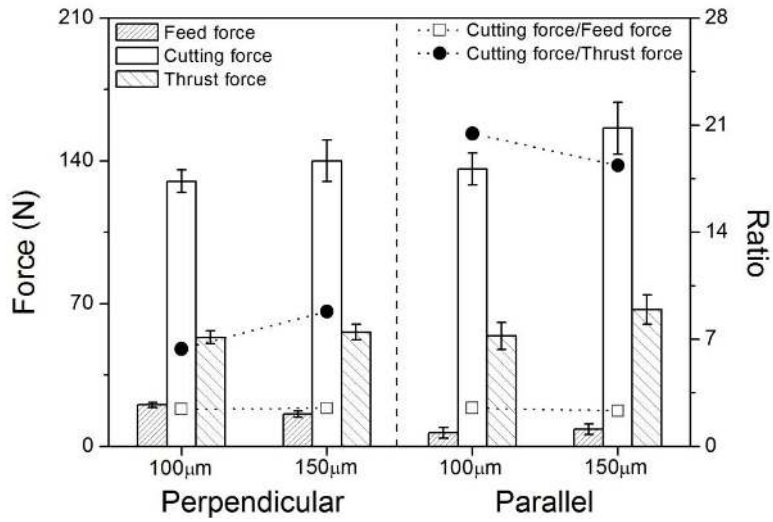
The cutting force and thrust force were lowest for an edge distance of 100 μm . This agreed with the experimental results of (Obikawa et al., 2011). Variation of the edge distance did not appear to have any effect on reducing the force (Fig. 4-4 (a)). However, an infinite edge distance with a textured tool decreased the thrust and cutting force again. The reason for such a high cutting force with a 50- μm edge distance is that the textured tool was not capable of cutting metal from a workpiece and generating a high distributed stress (Fig. 4-4 (b)). The feed force was opposite to the largest force at an edge distance of 100 μm (Fig. 4-4 (c)). Similarly, the shear stress was widely distributed in the chip and workpiece for edge distances of 100 and 150 μm (Fig. 4-4(d)). An edge distance of 300 μm (Fig. 4-4(e)) reduced the range of distributed stress.

There was no difference in the ratios for cutting force/feed force at both textures. The ratios for cutting force/thrust were increased with the perpendicular texture. The ratios for cutting force/thrust force with the perpendicular texture were reduced.

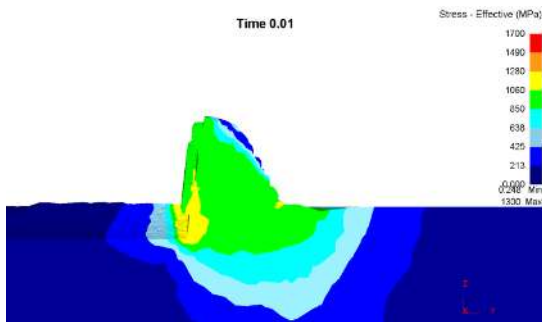
The chip flow angle varied along with the cutting force. The edge distance, chip flow direction, and cutting forces also varied proportionally. The cutting force was the least for an edge distance of 100 μm . The chip flow direction angle also decreased. For an edge distance of 50 μm , the chip flow direction was 116°; this was in a direction opposite to that in other simulations.



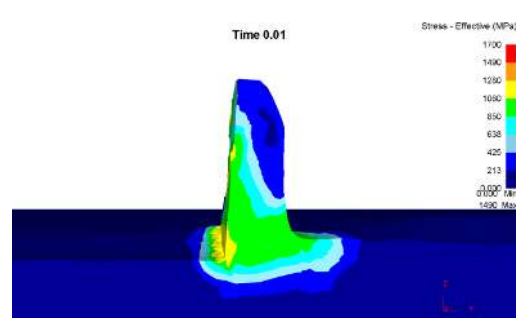
(a)



(b)

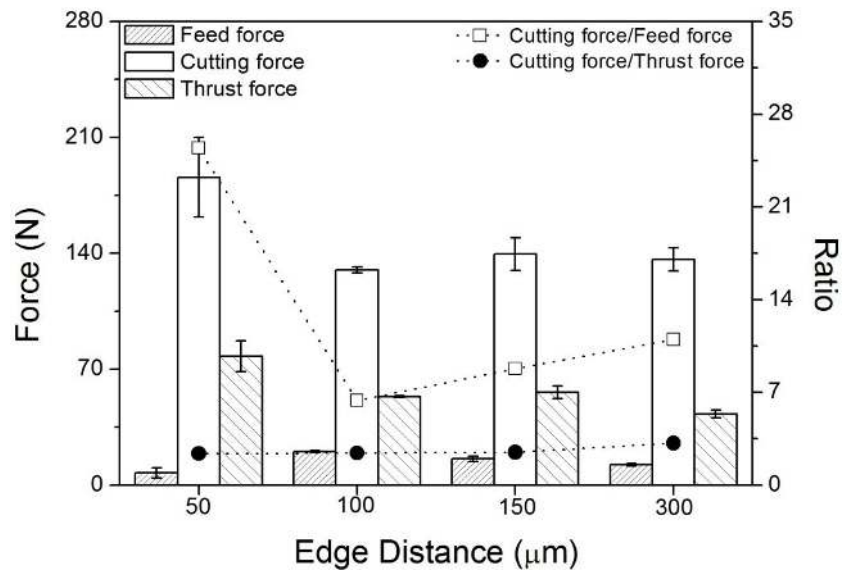


(c)

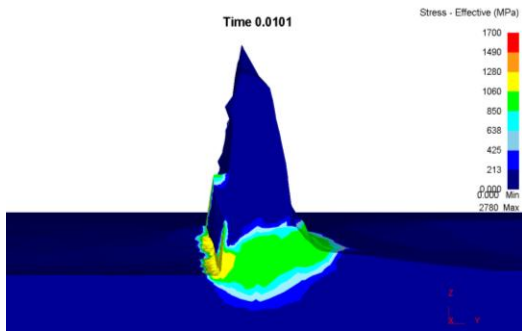


(d)

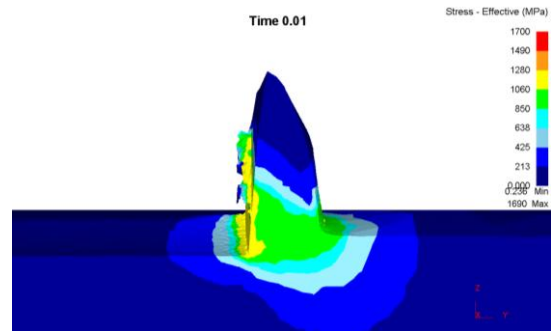
Fig. 4-3. (a) Quasi-steady-state area of the cutting force as a function of edge distance, and (b) predictive force and ratios (cutting force/feed force, cutting force/thrust force) for the perpendicular and parallel textures for edge distances of 100 and 150 μm . The effective stress of the workpiece cross-section on (c) a perpendicular tool with no edge and (d) a parallel tool with an edge distance of 150 μm .



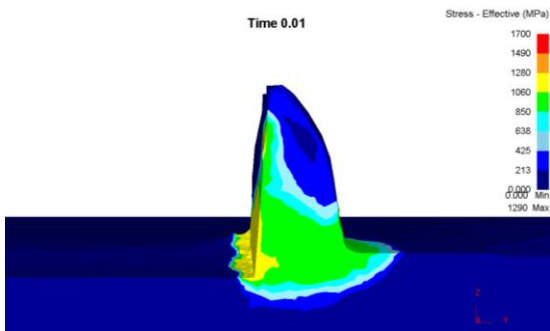
(a)



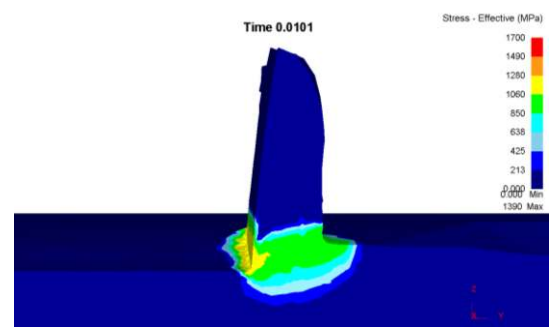
(b) 50 μm



(c) 100 μm



(d) 150 μm



(e) 300 μm

Fig. 4-4. (a) Predictive force and ratios (cutting force/feed force, cutting force/thrust force) for the perpendicular pattern as a function of edge distance. (b)–(e) Effective stress of the workpiece cross-section on a perpendicular tool as a function of the edge distance.

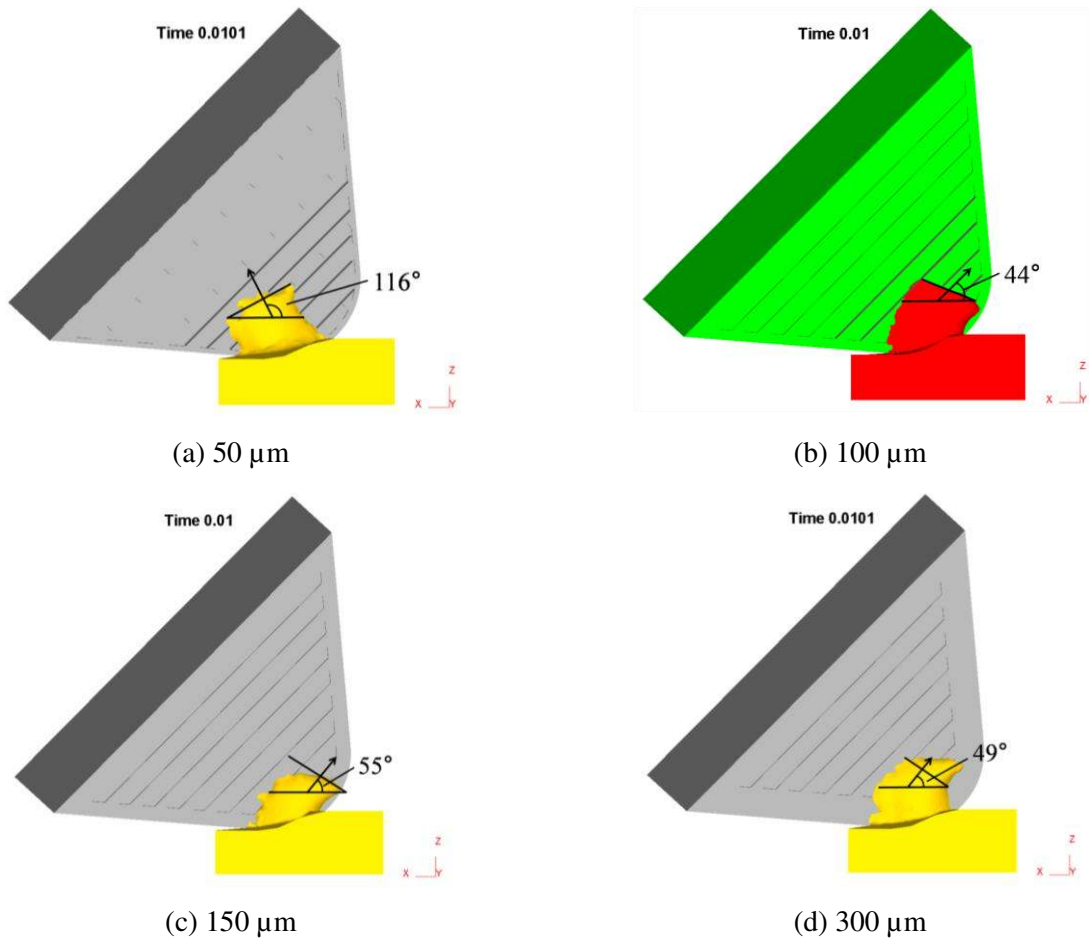


Fig. 4-5. Chip flow angle at edge distances of (a) 50 μm , (b) 100 μm , (c) 150 μm , and (d) 300 μm .

4.3 Pitch and height

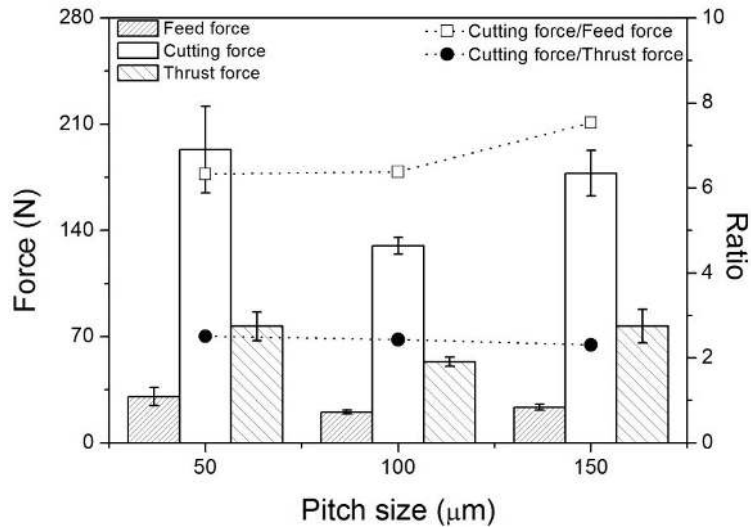
Figure 4-6 shows the various force and ratios as functions of pitch size for only the perpendicular pattern texture. The pitch size varied from 50 to 150 μm while the following parameters remained fixed: shear constant 0.6; edge distance, 100 μm ; and height, 50 μm .

All of the predictive forces were lowest for a pitch size of 100 μm . The distributed stress in the thrust direction had a greater range for heights of 50 and 150 μm (Figs. 4-6 (b)–(d)). The predictive force was largest at a pitch size of 50 μm . However, the experimental results (Obikawa et al., 2011, Kawasegi et al., 2009) indicated that the force diminished as the pitch size increased linearly. This was due to the different size effects in the experiments, most of which used pitch sizes that were less than 50 μm .

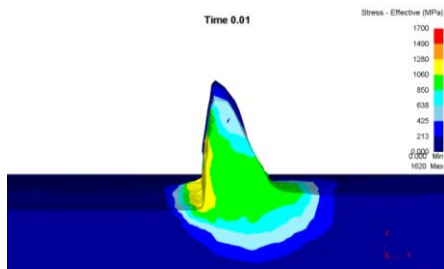
The ratio for the cutting force/thrust force reduced linearly despite the lowest cutting force, which occurred at a pitch size of 100 μm . The ratio for the cutting force/feed force increased as the ratio for the cutting force/thrust force diminished. In the experiments (Obikawa et al., 2011), the friction coefficient in the cutting direction increased as the pitch size increased. A very small pitch size increased the contact area, and thus increased the force. With large pitch sizes, the pattern had no effect on decreasing the force.

The chip flow angle was lowest and the predictive force was very large for a pitch size of 50 μm . When the chip flow angle increased, so did the predictive force.

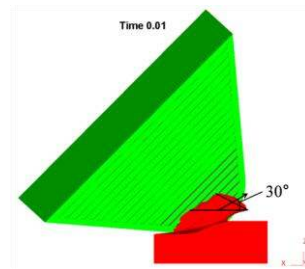
Figure 4-7 shows the predictive force and ratios for pattern heights of 50 and 100 μm . The cutting thrust forces increased as the heights increased, but the feed force decreased. The effective stress toward the thrust direction was greater for a height of 50 μm than for 100 μm . The chip flow angle decreased as the height increased. The experimental results (Obikawa et al., 2011, Kawasegi et al., 2009) showed the opposite tendency: the measured force decreased as the height increased. However, the height range in the simulation was greater than that of the experiment, which used heights of less than 10 μm .



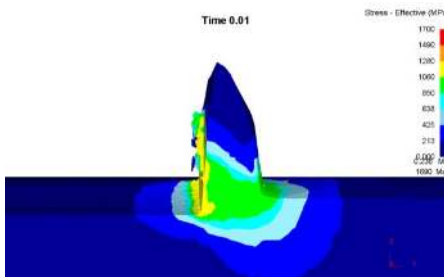
(a)



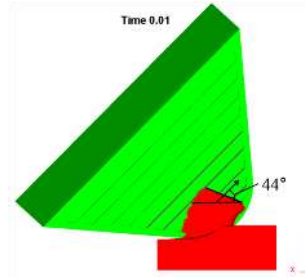
(b) $50 \mu\text{m}$



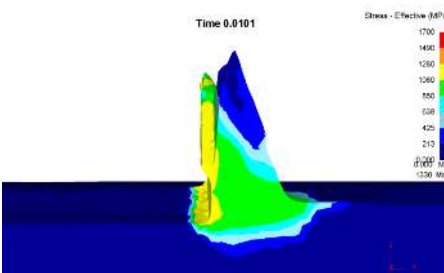
(e) $50 \mu\text{m}$



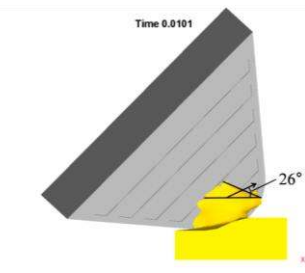
(c) $100 \mu\text{m}$



(f) $100 \mu\text{m}$

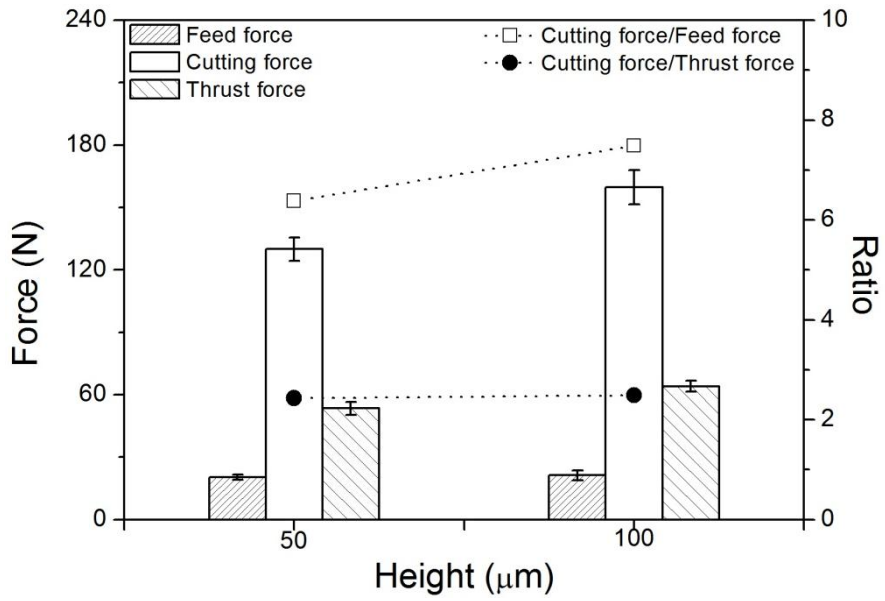


(d) $150 \mu\text{m}$

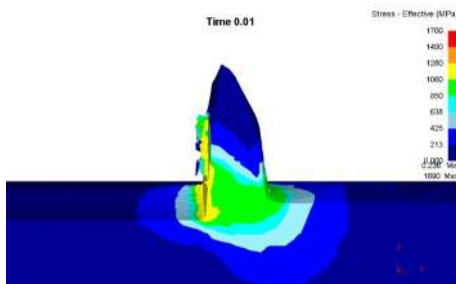


(g) $150 \mu\text{m}$

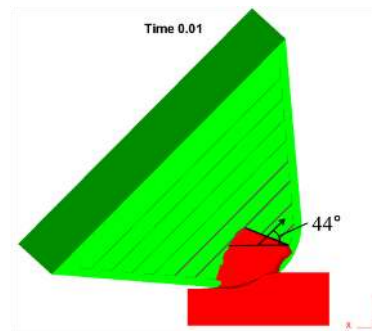
Fig. 4-6. (a) Effect of pitch size on the predictive force and ratios (cutting force/feed force, cutting force/thrust force). (b)–(d) Effective stress of the workpiece cross-section on a perpendicular tool as a function of pitch size. (e)–(g) Chip flow angle as a function of pitch size.



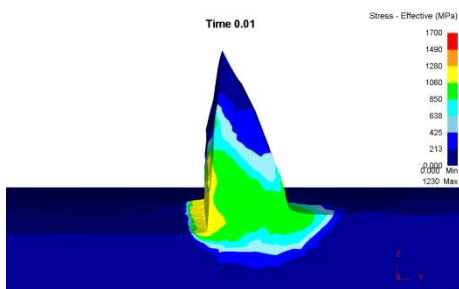
(a)



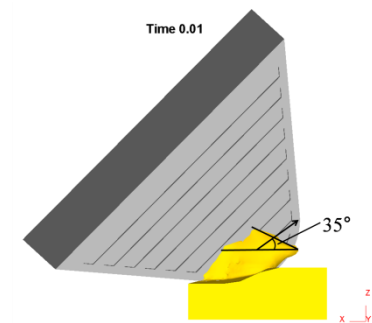
(b) 50 μm



(d) 50 μm



(c) 100 μm



(e) 100 μm

Fig. 4-7. (a) Effect of height on the predictive force and ratios (cutting force/feed force, cutting force/thrust force). (b), (c) Effective stress of the workpiece cross-section on a perpendicular tool as a function of height. (d), (e) Chip flow angle as a function of height.

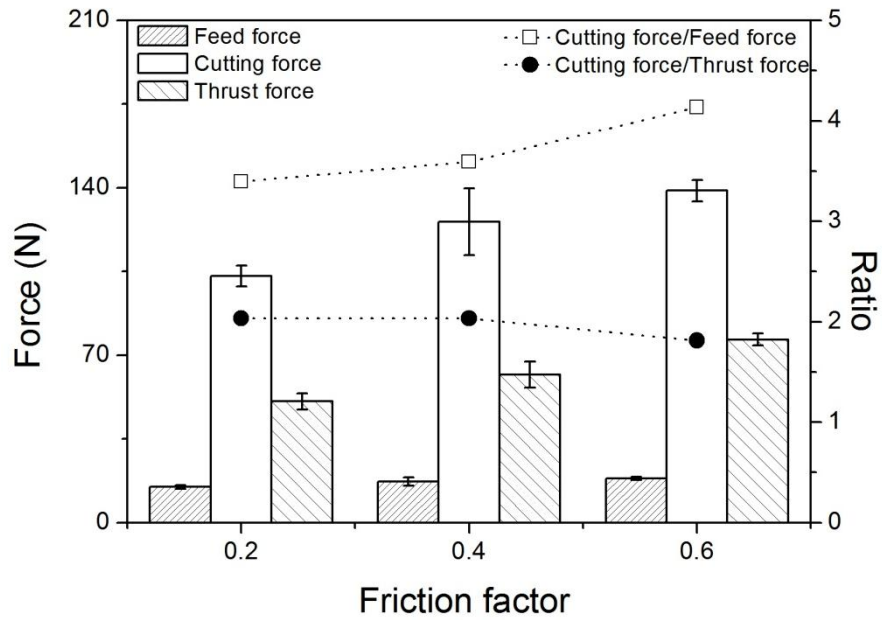
4.4 Friction factor

The shear friction constant was set to 0.2, 0.4, and 0.6 for each texture pattern. For the flat pattern (Fig. 4-8(a)), all of the predictive forces increased as the shear friction constant increased. The ratio for the cutting force/thrust force decreased, while that the ratio for the cutting force/feed force increased. When the shear constant changed from 0.4 to 0.6, the ratios for the cutting force/feed force increased dramatically, while that for the cutting force/thrust force decreased. For the perpendicular texture pattern (Fig. 4-8(b)), the thrust force increased with the shear factor, although the cutting force and feed force decreased. In particular, the cutting force decreased significantly as the shear factor increased from 0.4 to 0.6.

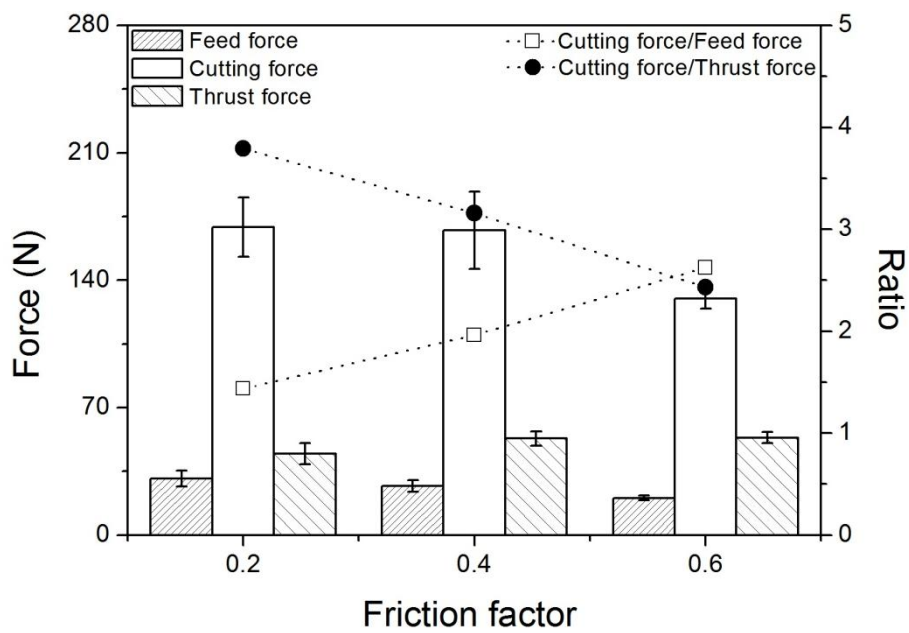
The parallel (Fig. 4-9 (a)) and rectangular (Fig. 4-9(b)) patterns had a similar tendency. The cutting force was very large for a shear factor of 0.4 in both cases. The cutting force increased significantly as the shear factor increased from 0.2 to 0.4. The ratio for the cutting force/feed force was larger than that for the cutting force/thrust force at shear factor 0.4 and 0.6. The feed force for the parallel texture pattern was not significantly affected by changes in the shear factor. The cutting force was very large for a shear factor of 0.4. The thrust force was the largest for a shear of 0.2. The ratio increased significantly in the cutting direction, and the ratios in the feed direction decreased linearly as the shear value increased. A shear factor of 0.6 was regarded as suitable for simulation of perpendicular texture patterns.

The rectangular texture pattern had a high force at a shear of 0.4, just like the parallel texture. The feed force was almost constant, independent of the shear, while the thrust changed significantly from a shear factor of 0.2 to 0.4. The cutting force also changed significantly at a shear factor of 0.4. The coefficient of friction ratio in the feed direction was largest at a shear factor of 0.2.

Figures 4-10 and 4-11 show the chip flow angle. The chip of the flat texture had the largest flow angle of all the texture types. In particular, for the flat texture, the chip flowed out at a shear factor of 0.2, as shown in Fig. 4-10(a). The increased friction values caused the chip to stick to the tool rake surface because the high shear stress held the chip, and the normal stress did not exist outside the depth of cut. The chip thickness increased slightly. The distributed stress of the perpendicular texture was wider than that of the flat texture. This is why the chip stuck to the surface of the tool rake. The parallel texture had a greater chip flow angle than the perpendicular texture did. The stress distribution range was small, similar to the flat texture for a shear factor of 0.2. The increased shear made the chip stick to the tool rake face, as it did for the perpendicular texture. Thus, the chip flow angles were reduced as the shear increased. The folding angle of the rectangular texture remained almost constant, independent of the shear value.

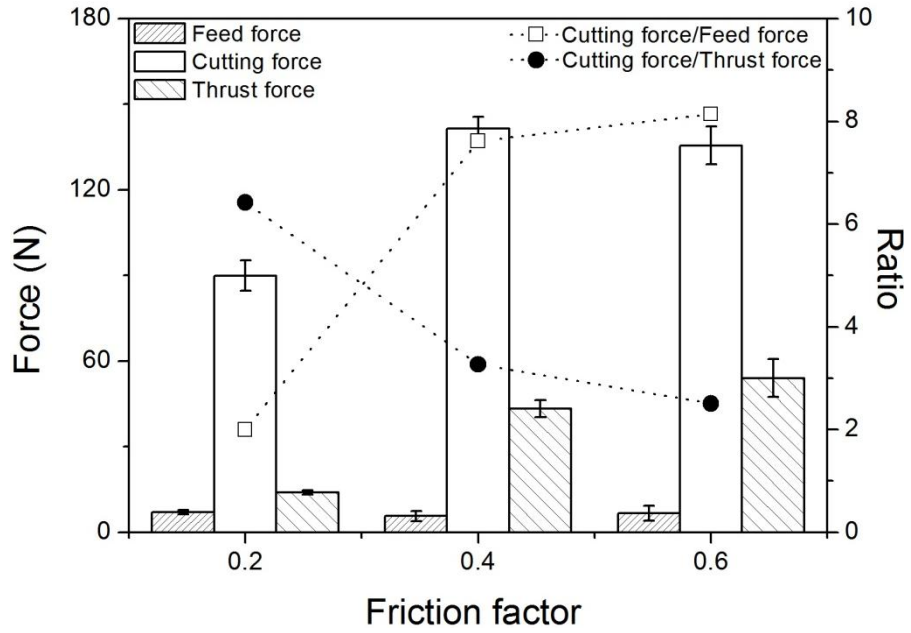


(a) flat

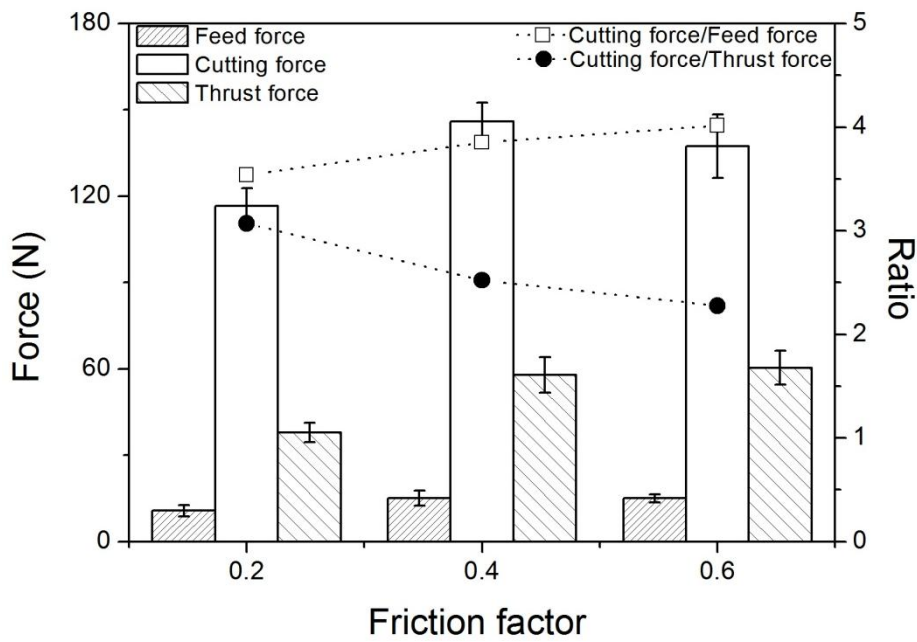


(b) perpendicular

Fig. 4-8. Predictive force and ratios (cutting force/feed force, cutting force/thrust force) (a) flat and (b) perpendicular texture patterns.

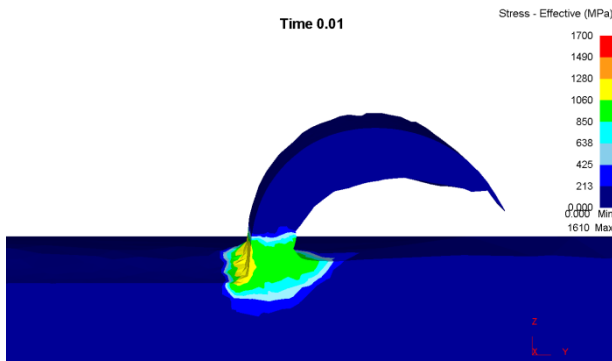


(a)

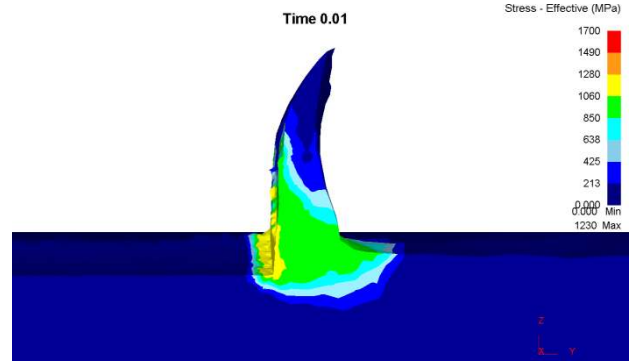


(b)

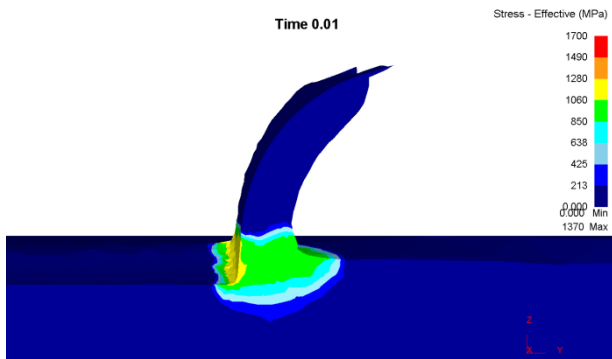
Fig. 4-9. Predictive force and ratios (cutting force/feed force, cutting force/thrust force)
 (a) parallel and (b) rectangular texture patterns.



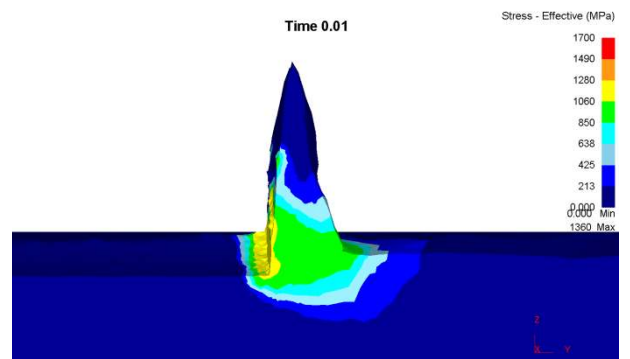
(a) shear factor = 0.2



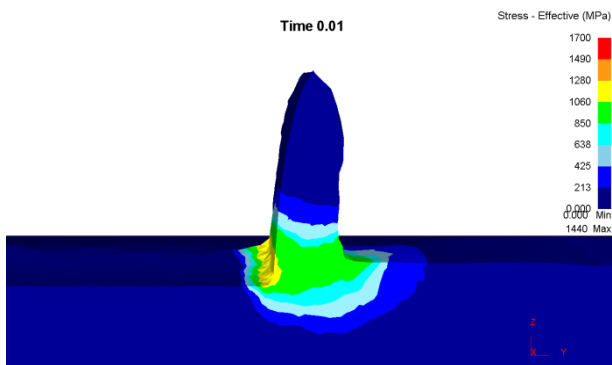
(d) shear factor = 0.2



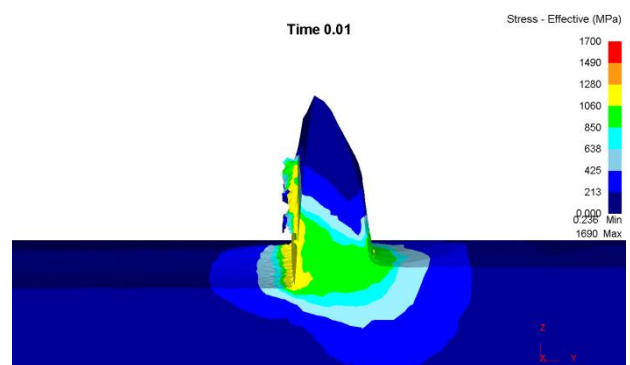
(b) shear factor = 0.4



(e) shear factor = 0.4

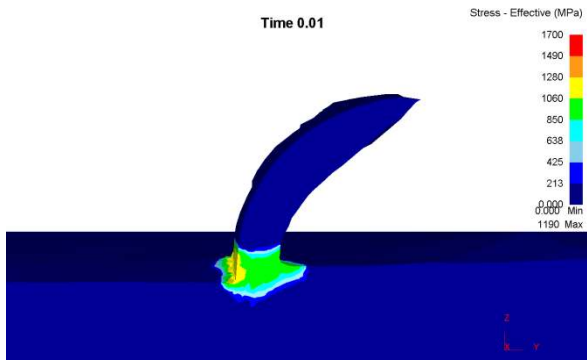


(c) shear factor = 0.6

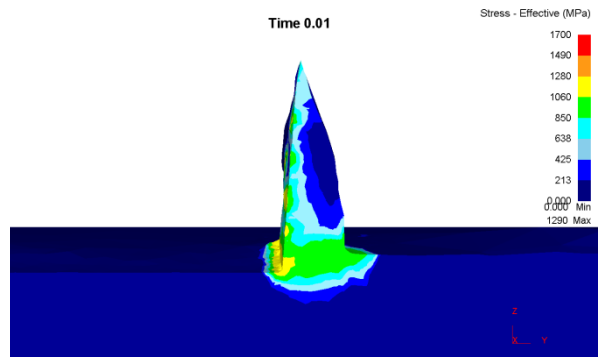


(f) shear factor = 0.6

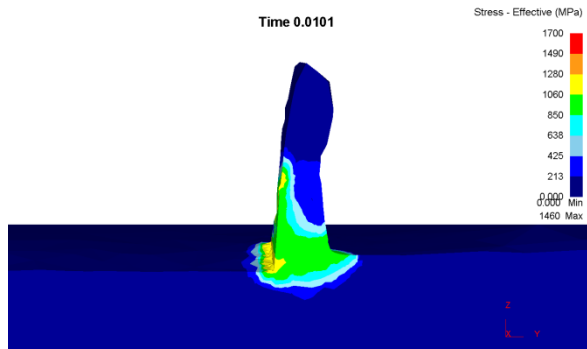
Fig. 4-10. Chip morphology and stress distribution for the (a)–(c) flat and (d)–(f) perpendicular textures.



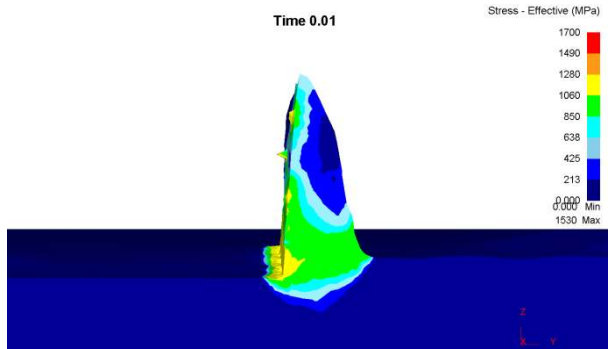
(a) shear factor = 0.2



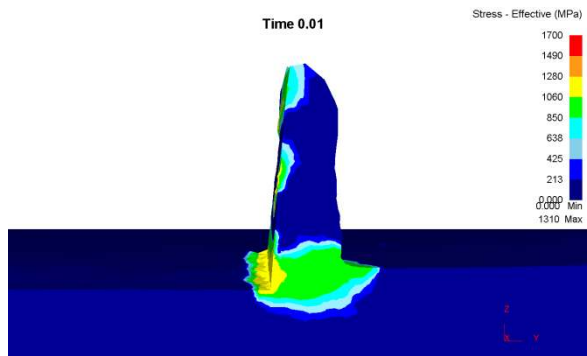
(d) shear factor = 0.2



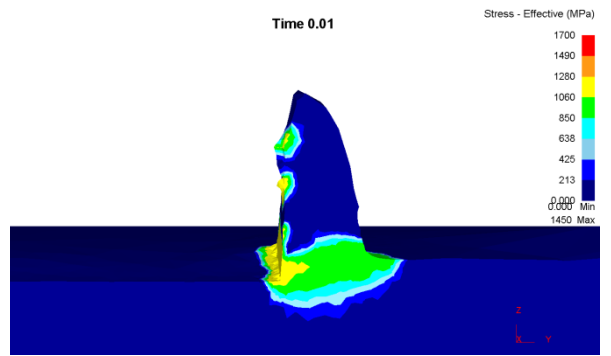
(b) shear factor = 0.4



(e) shear factor = 0.4



(c) shear factor = 0.6

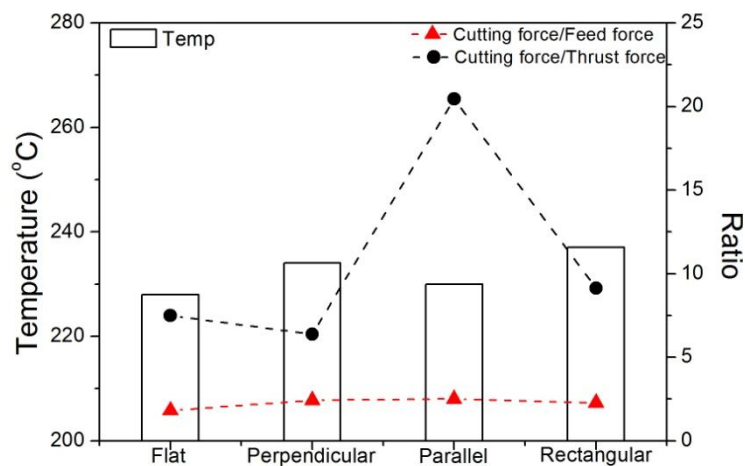


(f) shear factor = 0.6

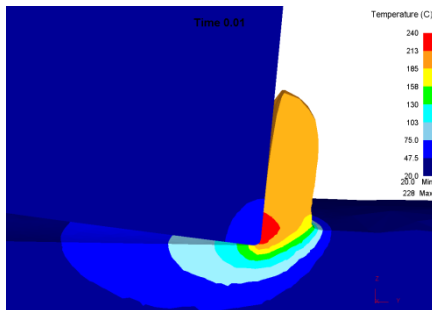
Fig. 4-11. Chip morphology and stress distribution for the (a)–(c) parallel and (d)–(f) rectangular textures.

4.5 Thermal effects and waviness on the chip

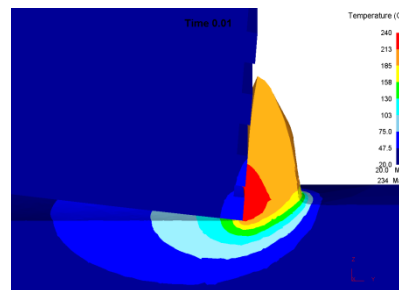
Figure 4-12 shows the thermal effects for each pattern type. The secondary heat sources generated the most heat, regardless of the pattern type. The temperature was the highest for the rectangular pattern, while the flat pattern had the lowest temperature because its contact area was the smallest. Figure 4-12(a) shows the relationship between the temperature and the ratios for the cutting force/feed force and the cutting force/thrust force.



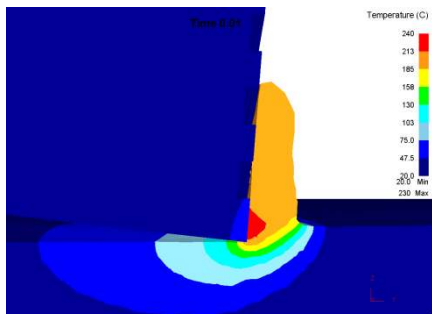
(a)



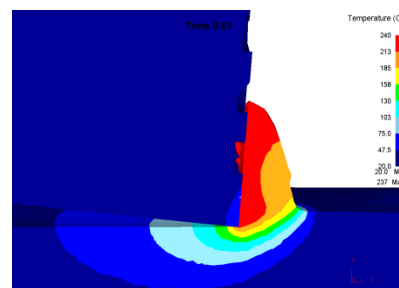
(b)



(c)



(d)



(e)

Fig. 4-12. (a) Predictive temperature and ratios (cutting force/feed force, cutting force/thrust force) for the (b) flat, (c) perpendicular, (d) parallel, and (e) rectangular textures.

The waviness of the texture is marked on the chip during metal machining, as shown by previous experiments (Kawasegi et al., 2009) and our FEM simulations. The stress is distributed by the texture, and leaves its imprint on the texture.

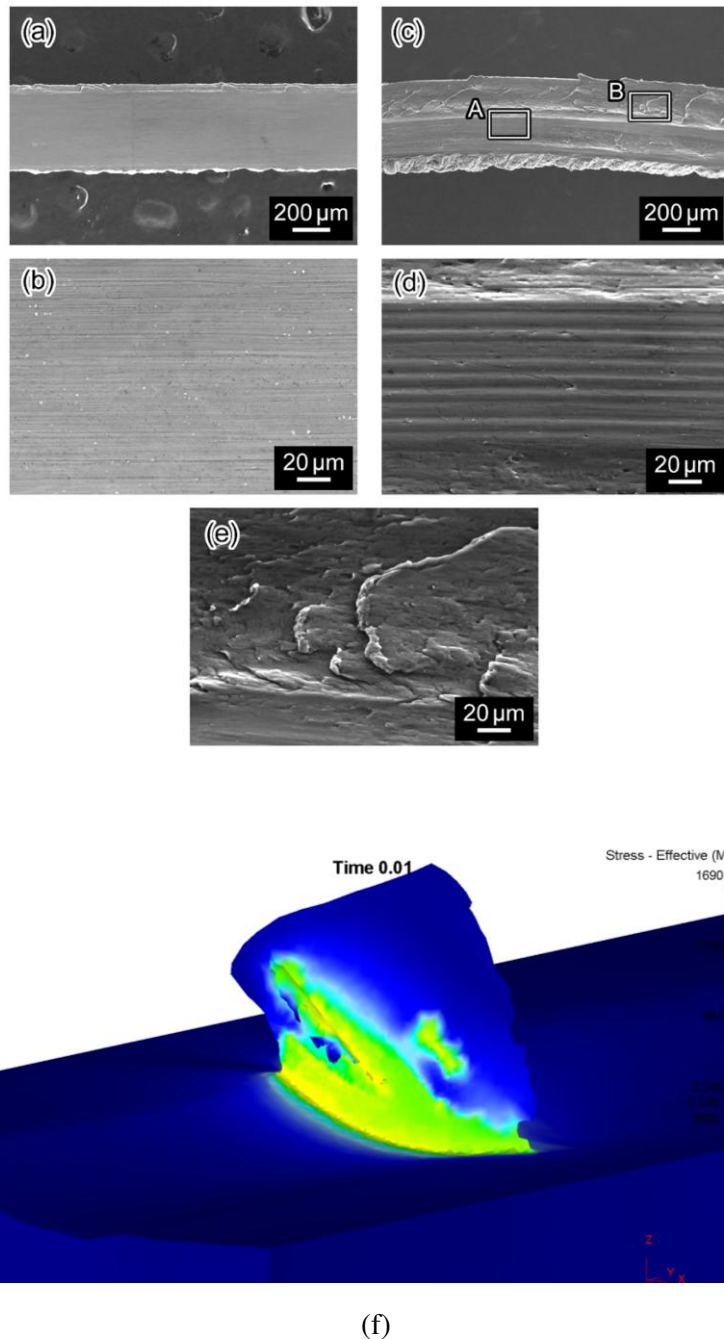


Fig. 4-13. Scanning electron microscopy images of chips generated while turning aluminum alloy under dry conditions showing (a) a nanotextured tool with perpendicular waviness and (b) an enlarged image of (a), and (c) a nanotextured tool with parallel waviness and (d, e) enlarged images indicated by A and B (Kawasegi et al., 2009). (f) Effective stress on the chip for the perpendicular texture.

4.6 Summary

This chapter described the simulation results for the effects of tool texturing. The four types of texture patterns were flat (non-textured), perpendicular, parallel, and rectangular. Because the perpendicular pattern gave the best results and had the lowest predictive force, it can be considered representative of all the experiments. However, the parallel pattern gave the poor results for the ratios, and its results were opposite to those of the others.

The simulations analyzed various edge distances for the perpendicular and parallel textures only. A tool with no edge, i.e., an edge distance of zero, had the highest predictive force. For the perpendicular texture, an increase in the edge distance increased the predictive force and the ratio. The parallel texture demonstrated the opposite tendency.

The pitch size and height of the texture pattern affected only the perpendicular texture. A pitch size of 100 μm reduced the predictive force. The ratio increased as the pitch size increased. An increase in height increased the predictive force and the ratio.

Changes in the shear friction affected all texture types. They increased the force for the flat pattern, and decreased the force for the perpendicular pattern. The parallel and rectangular textures had their largest forces at shear constants of 0.4. A shear constant of 0.6 was regarded as suitable for the simulation of textured tools.

The effective stress was widely distributed on the chip, the pattern had a high predictive force. Furthermore, the ratio was highest. The force affected the chip flow direction angle was in that when the pattern had a high force, the chip rotated to the pattern direction and the chip flow angle decreased.

5. CONCLUSIONS AND RECOMMENDATIONS

5.1 Summary of work

This dissertation was motivated by the need to reduce the friction of the tool–chip contact interface in hard turning. One way of reducing friction is to place a grooved pattern on the tool rake surface. Many experiment-based research efforts have shown that the measured force and friction are functions of lubrication. However, the objective of this study was to use FEM simulation to validate the effect of textured tools.

Chapter 2 presented a literature review on the theory of hard-turning modeling, application of the FEM for metal cutting, and experimental cases classified by fabrication method. The theory of the hard-turning process was discussed in terms of the cutting mechanism for the force and thermal effects. The basis of the FEM for metal was presented as an analysis algorithm for the DEFORM software, the criteria of chip separation, friction, and heat transfer. In addition, the textured tools from previous research were classified by fabrication method.

Chapter 3 discussed the preparation work for the simulation analysis and described the tool material properties and workpiece properties such as flow stress. Boundary conditions and mesh control were examined. The chapter also discussed the comparison of theoretical, simulation, and experimental data.

Chapter 4 discussed the results of the simulations in terms of the four texture shapes, edge distance, pitch size, pattern height, and friction factors.

5.2 Conclusions

The effects of four textures (flat, perpendicular, parallel, and rectangular) for hard turning were investigated using FEM with the aim of reducing friction. The textured tools had reduced predictive forces and ratios. The feed force had the opposite tendency to the cutting and thrust forces. The edge distance is an important parameter for cutting metal. In the case of no edge, i.e., edge distance of zero, the predictive force was extremely large because the maximum shear stress was not generated at the shear zone. An edge distance of 100 μm showed the most promise for reducing the predictive force.

The pitch size and pattern height affected the predictive force. A pitch size of 100 μm gave the best results, and decreased height tended to reduce the force. The ratio increased as the pitch size increased, and increased as the height increased.

A shear constant value of 0.6 was regarded as suitable for the simulation of textured tools. The chip flow angle was related to the predictive force.

5.3 Recommendations for future work

The simulation results showed that textured tools reduced the force, but not the friction coefficient. Because direct comparison with experimental results was somewhat difficult due to size differences, accurate comparison would require experiments and simulation to use the same conditions. In addition, simulation and experiments involving other cutting parameters, such as the surface velocity, depth of cut, and feed rate, should be conducted.

REFERENCE

- AL-ZKERI, I. 2005. STATE OF THE TECHNOLOGY IN HARD TURNING. Columbus, Ohio: The Ohio state University.
- AL-ZKERI, I. A. 2007. *Finite element modeling of hard turning*. Ohio State University.
- BLATTER, A., MAILLAT, M., PIMENOV, S. M., SHAFEEV, G. A., SIMAKIN, A. V. & LOUBNIN, E. N. 1999. Lubricated sliding performance of laser-patterned sapphire. *Wear*, 232, 226-230.
- BOOTHROYD, G. 1963. Temperatures in orthogonal metal cutting. *Proceedings of the Institution of Mechanical Engineers*, 177, 789-810.
- BRUZZONE, A. A. G., COSTA, H. L., LONARDO, P. M. & LUCCA, D. A. 2008. Advances in engineered surfaces for functional performance. *CIRP Annals - Manufacturing Technology*, 57, 750-769.
- CARROLL III, J. T. & STRENKOWSKI, J. S. 1988. Finite element models of orthogonal cutting with application to single point diamond turning. *International Journal of Mechanical Sciences*, 30, 899-920.
- CHILDS, T. H. C. 1998. MATERIAL PROPERTY NEEDS IN MODELING METAL MACHINING. *Machining Science and Technology*, 2, 303-316.
- CHILDS, T. H. C. & MAEKAWA, K. 1990. Computer-aided simulation and experimental studies of chip flow and tool wear in the turning of low alloy steels by cemented carbide tools. *Wear*, 139, 235-250.
- CHILDS, T. H. C., MAEKAWA, K., OBIKAWA, T., YAMANE, Y. 2000. *Metal Machining: Theory and Application*. London.
- COSTA, H. & HUTCHINGS, I. 2009. Effects of die surface patterning on lubrication in strip drawing. *Journal of Materials Processing Technology*, 209, 1175-1180.
- DAWSON, T. G. 2002. *Machining hardened steel with polycrystalline cubic boron nitride cutting tools*. Georgia Institute of Technology.
- DOGRA, M., SHARMA, V. S., SACHDEVA, A., SURI, N. M. & DUREJA, J. S. 2010. Tool Wear, Chip Formation and Workpiece Surface Issues in CBN Hard Turning: A Review. *International Journal of Precision Engineering and Manufacturing*, 11, 341-358.
- DUBRUJEAUD, B., VARDAVOULIAS, M. & JEANDIN, M. 1994. The role of porosity in the dry sliding wear of a sintered ferrous alloy. *Wear*, 174, 155-161.
- ERDEMIR, A. 2005. Review of engineered tribological interfaces for improved boundary lubrication.

- Tribology International*, 38, 249-256.
- EVANS, C. J. & BRYAN, J. B. 1999. "Structured", "Textured" or "Engineered" Surfaces. *CIRP Annals - Manufacturing Technology*, 48, 541-556.
- GUO, #160, B., Y., LIU & R., C. 2002. *3D FEA modeling of hard turning*, New York, NY, ETATS-UNIS, American Society of Mechanical Engineers.
- HASAN, R. 1998. Why are you still grinding? *Manufacturing Engineering(USA)*, 120, 76.
- HEATH, P. 1987. Properties and uses of Amborite. *Carbide Tool J.*, 19, 12-14.
- HINTZE W., E. A., AND WURFELS K. . 1998. *Tool for material removal machining*. US patent application.
- HUANG, Y. 2002. *Predictive Modeling of Tool Wear Rate with Applications to CBN Hard Turning*. PhD Dissertation, Georgia Institute of Technology.
- HUANG, Y. & LIANG, S. Y. 2003. Cutting forces modeling considering the effect of tool thermal property - application to CBN hard turning. *International Journal of Machine Tools & Manufacture*, 43, 307-315.
- JIANXIN, D., ZE, W., YUNSONG, L., TING, Q. & JIE, C. 2012. Performance of carbide tools with textured rake-face filled with solid lubricants in dry cutting processes. *International Journal of Refractory Metals and Hard Materials*, 30, 164-172.
- JOHNSON, G. R. & COOK, W. H. Year. A constitutive model and data for metals subjected to large strains, high strain rates and high temperatures. *In*, 1983. The Hague, Netherlands: International Ballistics Committee, 541-547.
- KAWASEGI, N., SUGIMORI, H., MORIMOTO, H., MORITA, N. & HORI, I. 2009. Development of cutting tools with microscale and nanoscale textures to improve frictional behavior. *Precision Engineering*, 33, 248-254.
- KOMVOPOULOS, #160, K., ERPENBECK & A., S. 1991. *Finite element modeling of orthogonal metal cutting*, New York, NY, ETATS-UNIS, American Society of Mechanical Engineers.
- KOMVOPOULOS, K. & ERPENBECK, S. A. 1991. Finite element modeling of orthogonal metal cutting. *Journal of engineering for industry*, 113, 253-267.
- KONIG, W., BERKTOLD, A., KOCH, K.F. 1984. *Machining of Hard Materials*, Annals of CIRP.
- MACGINLEY, T. & MONAGHAN, J. 2001. Modelling the orthogonal machining process using coated cemented carbide cutting tools. *Journal of Materials Processing Technology*, 118, 293-300.
- MAMALIS, A. G., BRANIS, A. S. & MANOLAKOS, D. E. 2002. Modelling of precision hard cutting using implicit finite element methods. *Journal of Materials Processing Technology*, 123, 464-475.
- MAMALIS, A. G., HORV TH, M., BRANIS, A. S. & MANOLAKOS, D. E. 2001. Finite element simulation of chip formation in orthogonal metal cutting. *Journal of Materials Processing*

- Technology*, 110, 19-27.
- MCCLINTOCK, F. A. 1968. A Criterion for Ductile Fracture by the Growth of Holes. *Journal of Applied Mechanics*, 35, 363-371.
- MERCHANT, M. E. 1945. Mechanics of the metal cutting process. II. Plasticity conditions in orthogonal cutting. *Journal of Applied Physics*, 16, 318-324.
- NG, E. G., ASPINWALL, D. K., BRAZIL, D. & MONAGHAN, J. 1999. Modelling of temperature and forces when orthogonally machining hardened steel. *International Journal of Machine Tools & Manufacture*, 39, 885-903.
- OBIKAWA, T., KAMIO, A., TAKAOKA, H. & OSADA, A. 2011. Micro-texture at the coated tool face for high performance cutting. *International Journal of Machine Tools and Manufacture*, 51, 966-972.
- OXLEY, P. L. B. 1989. Mechanics of Machining: an Analytical Approach to Assessing Machinability.(Retroactive Coverage). *Ellis Horwood Limited(UK)*, 1989, 242.
- ÖZEL, T. 2006. The influence of friction models on finite element simulations of machining. *International Journal of Machine Tools and Manufacture*, 46, 518-530.
- PETTERSSON, U. & JACOBSON, S. 2006. Tribological texturing of steel surfaces with a novel diamond embossing tool technique. *Tribology International*, 39, 695-700.
- RAMESH, A., MELKOTE, S. N., ALLARD, L. F., RIESTER, L. & WATKINS, T. R. 2005. Analysis of white layers formed in hard turning of AISI 52100 steel. *Materials Science and Engineering: A*, 390, 88-97.
- SFTC 2008. DEFORM 3D User's Manual. Clolumbus, Ohio: Scientific Forming Technology Co.
- STABLER, G. 1951. The fundamental geometry of cutting tools. *Proceedings of the Institution of Mechanical Engineers*, 165, 14-26.
- STENKOWSKI, #160, S., J. & MOON, K.-J. 1990. *Finite element prediction of chip geometry and tool/workpiece temperature distributions in orthogonal metal cutting*, New York, NY, ETATS-UNIS, American Society of Mechanical Engineers.
- SUBBIAH, S. 2006. Some investigations of scaling effects in micro-cutting.
- SUGIHARA, T. & ENOMOTO, T. 2009. Development of a cutting tool with a nano/micro-textured surface—Improvement of anti-adhesive effect by considering the texture patterns. *Precision Engineering*, 33, 425-429.
- TATSUMI, T., TAKEDA, J., IMAI, K. & HASHIMOTO, H. 1999. *An engineered tool and some results of fly-cut experiments*, Aachen, Shaker Verlag GmbH.
- UEDA, K. & MANABE, K. 1993. Rigid-Plastic FEM Analysis of Three-Dimensional Deformation Field in Chip Formation Process. *CIRP Annals - Manufacturing Technology*, 42, 35-38.
- UMBRELLLO, D., HUA, J. & SHIVPURI, R. 2004. Hardness-based flow stress and fracture models for numerical simulation of hard machining AISI 52100 bearing steel. *Materials Science and*

Engineering: A, 374, 90-100.

- WAKUDA, M., YAMAUCHI, Y., KANZAKI, S. & YASUDA, Y. 2003. Effect of surface texturing on friction reduction between ceramic and steel materials under lubricated sliding contact. *Wear*, 254, 356-363.
- XIE, J., LUO, M. J., HE, J. L., LIU, X. R. & TAN, T. W. 2012. Micro-grinding of micro-groove array on tool rake surface for dry cutting of titanium alloy. *International Journal of Precision Engineering and Manufacturing*, 13, 1845-1852.
- ZHANG, B. & BAGCHI, A. 1994. Finite Element Simulation of Chip Formation and Comparison with Machining Experiment. *Journal of engineering for industry*, 116, 289-297.
- ZHANG, J. 2005a. *Process Optimization for Machining of hardend Steels*. Doctor of Philosophy Georgia Institute of Technology.
- ZHANG, J. Y. 2005b. *Process optimization for machining of hardened steels*. Georgia Institute of Technology.
- ZHOU, J. M., WALTER, H., ANDERSSON, M. & STAHL, J. E. 2003. Effect of chamfer angle on wear of PCBN cutting tool. *International Journal of Machine Tools and Manufacture*, 43, 301-305.
- ZOREV, N. 1963. Inter-relationship between shear processes occurring along tool face and shear plane in metal cutting. *International Research in Production Engineering*, 49.

ACKNOWLEDGEMENTS

Above all, I would like to thank advisor Dr. Hyung Wook Park for his extensive support, guidance throughout the master course. I would also like to thank the committee members, Dr. Young Bin Park, Dr. Duck Young Kim for their suggestion during master course.

I would like to thank whole labmates in Multi-scale Hybrid Manufacturing Laboratory; Dr. Deka, Kyoung Il Kong, En Ju Park, Hyun Myoung Kim, Ji Su Kim, In Un Lee, and Jae Woo Seo for their assistance.

Finally, I would like to thank my parents and my little sister; Mi Young Kim for their love, assistance, encouragement during the master course. I would like to dedicate this thesis to my family.

